

# Spitzer Observations of M33 and the Hot Star, H II Region Connection

Robert H. Rubin<sup>1,2</sup>, Janet P. Simpson<sup>1,3</sup>, Sean W.J. Colgan<sup>1</sup>, Reginald J. Dufour<sup>4</sup>, Gregory Brunner<sup>4</sup>, Ian A. McNabb<sup>1</sup>, Adalbert W.A. Pauldrach<sup>5</sup>, Edwin F. Erickson<sup>1</sup>, Michael R. Haas<sup>1</sup>, and Robert I. Citron<sup>1</sup>

[rubin@cygnus.arc.nasa.gov](mailto:rubin@cygnus.arc.nasa.gov)

April 5, 2008

## ABSTRACT

We have observed emission lines of [S IV] 10.51, H(7–6) 12.37, [Ne II] 12.81, [Ne III] 15.56, and [S III] 18.71  $\mu\text{m}$  in a number of extragalactic H II regions with the *Spitzer Space Telescope*. A previous paper presented our data and analysis for the substantially face-on spiral galaxy M83. Here we report our results for the local group spiral galaxy M33. The nebulae selected cover a wide range of galactocentric radii ( $R_G$ ). The observations were made with the Infrared Spectrograph with the short wavelength, high resolution module. The above set of five lines is observed cospatially, thus permitting a reliable comparison of the fluxes. From the measured fluxes, we determine the ionic abundance ratios including Ne<sup>++</sup>/Ne<sup>+</sup>, S<sup>3+</sup>/S<sup>++</sup>, and S<sup>++</sup>/Ne<sup>+</sup> and find that there is a correlation of increasingly higher ionization with larger  $R_G$ . By sampling the dominant ionization states of Ne (Ne<sup>+</sup>, Ne<sup>++</sup>) and S (S<sup>++</sup>, S<sup>3+</sup>) for H II regions, we can estimate the Ne/H, S/H, and Ne/S ratios. We find from linear least-squares fits that there is a decrease in metallicity with increasing  $R_G$ :  $d \log (\text{Ne}/\text{H})/dR_G = -0.058 \pm 0.014$  and  $d \log (\text{S}/\text{H})/dR_G = -0.052 \pm 0.021 \text{ dex kpc}^{-1}$ . There is no apparent variation in the Ne/S ratio with  $R_G$ . Unlike our previous similar study of M83, where we conjectured that this ratio was an upper limit, for M33 the derived ratios are likely a robust indication of Ne/S. This occurs because

---

<sup>1</sup>NASA/Ames Research Center, Moffett Field, CA 94035-1000, USA

<sup>2</sup>Orion Enterprises, M.S. 245-6, Moffett Field, CA 94035-1000, USA

<sup>3</sup>SETI Institute, 515 N. Whisman Road, Mountain View, CA 94043, USA

<sup>4</sup>Physics & Astronomy Department, Rice University, MS 61, Houston, TX 77005-1892, USA

<sup>5</sup>University of Munich, Munich D-81679, Germany

the H II regions have lower metallicity and higher ionization than those in M83. Both Ne and S are primary elements produced in  $\alpha$ -chain reactions, following C and O burning in stars, making their yields depend very little on the stellar metallicity. Thus, it is expected that Ne/S remains relatively constant throughout a galaxy. The median (average) Ne/S ratio derived for H II regions in M33 is 16.3 (16.9), just slightly higher than the Orion Nebula value of 14.3. The same methodology is applied to *Spitzer* observations recently published for three massive H II regions: NGC 3603 (Milky Way), 30 Dor (LMC), and N 66 (SMC) as well as for a group of blue compact dwarf galaxies. We find median Ne/S values of 14.6, 11.4, 10.1, and 14.0, respectively. All of these values are in sharp contrast with the much lower “canonical”, but controversial, solar value of  $\sim 5$ . A recent nucleosynthesis, galactic chemical evolution (GCE) model predicts a Ne/S abundance of  $\sim 9$ . Our observations may also be used to test the predicted ionizing spectral energy distribution of various stellar atmosphere models. We compare the ratio of fractional ionizations  $\langle \text{Ne}^{++} \rangle / \langle \text{S}^{++} \rangle$ ,  $\langle \text{Ne}^{++} \rangle / \langle \text{S}^{3+} \rangle$ , and  $\langle \text{Ne}^{++} \rangle / \langle \text{Ne}^+ \rangle$  vs.  $\langle \text{S}^{3+} \rangle / \langle \text{S}^{++} \rangle$  with predictions made from our photoionization models using several of the state-of-the-art stellar atmosphere model grids. The trends of the ionic ratios established from the prior M83 study are remarkably similar, but continued to higher ionization with the present M33 objects.

*Subject headings:* ISM: abundances, H II regions, stars: atmospheres, galaxies: individual (M33)

## 1. Introduction

This work is a continuation of a similar previous study of 24 H II regions in the substantially face-on spiral galaxy M83 that we observed with the *Spitzer Space Telescope* (Rubin et al. 2007, hereafter R07). Here we present our more recent *Spitzer* observations of 25 H II regions in the local group spiral galaxy M33. The analyses of the new set, in conjunction with the M83 set, further elucidate topics investigated in R07. Since this paper should stand alone, that is, not require the reader to fully read R07 first, much of the material presented there is repeated here. At times, this may be verbatim.

Most observational studies of the chemical evolution of the universe rest on emission line objects, which define the mix of elemental abundances at advanced stages of evolution as well as the current state of the interstellar medium (ISM). Gaseous nebulae are laboratories for understanding physical processes in all emission-line sources and probes for stellar, galactic,

and primordial nucleosynthesis. *Spitzer* has a unique ability to address the abundances of the elements neon and sulfur. This is particularly true in the case of H II regions, where one can observe simultaneously four emission lines that probe the dominant ionization states of Ne ( $\text{Ne}^+$  and  $\text{Ne}^{++}$ ) and S ( $\text{S}^{++}$  and  $\text{S}^{3+}$ ). The four lines, [Ne II] 12.81, [Ne III] 15.56, [S III] 18.71, and [S IV] 10.51  $\mu\text{m}$  can be observed cospatially with the Infrared Spectrograph (IRS) on the *SST*. Because of the sensitivity of *SST*, the special niche, relative to previous (and near-term foreseeable) instruments, is for studies of extragalactic H II regions. Toward this end, we have used *SST* to observe  $\sim$ 25 H II regions each in galaxies with various metallicities and other properties. To the extent that all the major forms of Ne and S are observed, the true Ne/S abundance ratio could be inferred. For Ne, this is a safe assumption, but for S, there is the possibility of non-negligible contributions due to  $\text{S}^+$  as well as what could be tied up in molecules and dust. Due to this, we surmised that the large values derived for Ne/S for the M83 H II regions, which are fairly low ionization, were in fact *upper limits*. With a portion of our Cycle 2 *SST* observations of M33 H II regions in hand, we concluded that the preliminary Ne/S results (from  $\sim$ 12 to 21) were likely a reliable estimate because these nebulae had lower metallicity and much higher ionization than those in M83 (R07, Rubin et al. 2006).

The preliminary M33 Ne/S ratios and the Orion Nebula value of 14.3 (Simpson et al. 2004) were in sharp contrast with the much lower “canonical” solar value ( $\sim$ 5) (Lodders 2003; Asplund, Grevesse, & Sauval 2005). There was an even larger difference compared with the Ne/S ratio predicted by GCE models. According to calculations based on the theoretical nucleosynthesis, galactic chemical evolution models of Timmes, Woosley, & Weaver (1995), the Ne/S ratio in the solar neighborhood would change little, from 3.80 to 3.75, between solar birth and the present time (apropos for the Orion Nebula). These calculations were provided by Frank Timmes (private communication). Timmes noted that although massive stars are expected to dominate the Ne and S production (and are all that were included in their non-rotating models with no wind losses), there is likely to be some re-distribution of Ne and S from rotation or from Wolf-Rayet phases of evolution, along with contributions of Ne from novae or even heavier intermediate mass stars. Hence, the Ne/S of 3.8 should be considered a lower bound because some potential sources of Ne are missing. With *SST* observations such as we have undertaken for M83 and M33, there is important feedback to the GCE field.

The presence of radial (metal/H) abundance gradients in the plane of the Milky Way is well established in both gaseous nebulae and stars (e.g., Henry & Worthey 1999; Rolleston et al. 2000). Radial abundance gradients seem to be ubiquitous in spiral galaxies, though the degree varies depending on a given spiral’s morphology and luminosity class. The gradients are generally attributed to the radial dependence of star formation history

and ISM mixing processes (e.g., Shields 2002). Thus, the observed gradients are another tool for understanding galactic evolution (e.g., Hou et al. 2000; Chiappini et al. 2001; Chiappini et al. 2003). The premise is that star formation and chemical enrichment begins in the nuclear bulges of the galaxies and subsequently progresses outward into the disk, which has remained gas-rich. The higher molecular gas density in the inner regions produces a higher star formation rate, which results in a relatively greater return to the ISM of both “primary”  $\alpha$ -elements (including O, Ne, and S) from massive star supernovae, and “secondary” elements like N. Secondary nitrogen is produced by CNO burning of already existing carbon and oxygen in intermediate-mass stars and is subsequently returned to the ISM through mass loss. However, because chemical evolution models have uncertain input parameters, and because details of the abundance variations of each element are uncertain, current understanding of the formation and evolution of galaxies suffers (e.g., Pagel 2001).

Studies of H II regions in the Milky Way are hampered by interstellar extinction. For the most part, optical studies (e.g., Shaver et al. 1983) have been limited to those H II regions at galactocentric radius  $R_G \gtrsim 6$  kpc (predicated on  $R_\odot = 8$  kpc) because H II regions are very concentrated to the Galactic plane. Here extinction becomes severe with increasing distance from Earth. Observations using far-infrared (FIR) emission lines have penetrated the  $R_G \lesssim 6$  kpc barrier. Surveys with the *Kuiper Airborne Observatory (KAO)* by Simpson et al. (1995), Afflerbach et al. (1997), and Rudolph et al. (2006) have observed 16 inner Galaxy H II regions. With the *Infrared Space Observatory (ISO)*, Martín-Hernández et al. (2002a) observed 13 inner Galaxy H II regions covering FIR and also mid-IR lines. A major finding of these studies is that inner Galaxy H II regions generally have lower excitation (ionization) compared to those at larger  $R_G$ . This holds for both heavy element ionic ratios  $O^{++}/S^{++}$  (Simpson et al. 1995) and  $Ne^{++}/Ne^+$  (Simpson & Rubin 1990; Giveon et al. 2002), and also  $He^+/H^+$  measured from radio recombination lines (Churchwell et al. 1978; Thum, Mezger, & Pankonin 1980). Whether the observed increase in excitation with increasing  $R_G$  comes entirely from heavy element opacity effects in the H II regions and stellar atmospheres, or also from a gradient in the maximum stellar effective temperature,  $T_{\text{eff}}$ , of the exciting stars is still a point of controversy (e.g., Giveon et al. 2002; Martín-Hernández et al. 2002b; Smith, Norris, & Crowther 2002; Morisset et al. 2004).

It has become clear that nebular plasma simulations with photoionization modeling codes are enormously sensitive to the ionizing spectral energy distribution (SED) that is input (e.g., R07 and Simpson et al. 2004, and references in each). These SEDs need to come from stellar atmosphere models. In R07, we developed new observational tests of and constraints on the ionizing SEDs that are predicted from various stellar atmosphere models. We compared our *SST* observations of H II regions in M83 with the various tracks predicted from photoionization models that changed *only the ionizing SEDs*. M83 provided data for

high metallicity (at least twice solar, e.g., Dufour et al. 1980; Bresolin & Kennicutt 2002) and lower-ionization H II regions. The best overall fit to the nebular models was obtained using the supergiant stellar atmosphere models computed with the WM-BASIC code (Pauldrach, Hoffmann, & Lennon 2001; Sternberg, Hoffmann, & Pauldrach 2003).

We discuss the M33 *SST/IRS* observations in section 2. In section 3, the data are used to test for a variation in the degree of ionization of the H II regions with  $R_G$ . We examine the Ne/S abundance ratio for our M33 H II region sample in section 4. In section 5, we test for a variation in the Ne/H and S/H ratio with  $R_G$ . Section 6 describes how these *Spitzer* data are used to constrain and test the ionizing SEDs predicted by stellar atmosphere models. In section 7, there is additional discussion pertaining to the Ne/S ratio. Last, we provide a summary and conclusions in section 8.

## 2. *Spitzer Space Telescope Observations*

In the substantially face-on (tilt 56°) local group, spiral galaxy M33, we observed 25 H II regions, covering a wide range of deprojected galactocentric radii ( $R_G$ ) from 0.71 to 6.73 kpc. We used the *SST/IRS* in the short wavelength, high dispersion (spectral resolution  $\sim 600$ ) configuration, called the short-high (SH) module (e.g., Houck et al. 2004). This covers the wavelength range from 9.9 – 19.6  $\mu\text{m}$  permitting cospatial observations of all five of our programme emission lines: [S IV] 10.51, hydrogen H(7–6) ( $\text{H}\alpha$ ) 12.37, [Ne II] 12.81, [Ne III] 15.56, and [S III] 18.71  $\mu\text{m}$ .

The data were collected under the auspices of Spitzer programme identification 20057. Most of the observations were made in 2006, January 15 to February 1 (UT) during *SST/IRS* campaign 28. The last set of observations, one Astronomical Observing Request (AOR) out of a total of 8, was made on 2007, February 11 during *SST/IRS* campaign 38. Figure 1 shows the regions and apertures observed, while Table 1 lists the H II region positions and the aperture grid configuration used to observe each. The nebulae are designated by their BCLMP number (Boulesteix et al. 1974). The H II regions observed in the remaining AOR in 2007 were #62, 302, 691, 651, and 740W. The size of the SH aperture is 11.3'' $\times$ 4.7''. Maps were arranged with the apertures overlapping along the direction of the long slit axis (the “parallel” direction). The purpose of overlapping is that most spatial positions will be covered in at least two locations on the array, minimizing the effects of bad detectors. In the direction of the short slit axis (the “perpendicular” direction), the apertures were arranged immediately abutting each other; that is, with no overlap or space between them. In all cases, we chose the mapping mode with aperture grid patterns varying from a 1 $\times$ 2 grid to as large as a 2 $\times$ 4 grid in order to cover the bulk of the expected emission.

Our terminology for the aperture grid pattern is intended to give roughly the map size in integer multiples of the parallel  $\times$  perpendicular direction aperture size. For instance the  $1 \times 2$  and  $1 \times 3$  patterns have a shift of  $3.45''$  in the parallel direction and a  $4.7''$  shift in the perpendicular direction. The resulting map has a full size in the parallel direction of  $14.75''$  ( $11.3 + 3.45$ ) which is closest to the integer one in the parallel direction. For the two other aperture grid patterns used, the  $2 \times 3$  and  $2 \times 4$  patterns, the shift (or step) is  $3.77''$  ( $1/3$  the aperture length) in the parallel direction. Thus, the resulting maps have a full size that covers an area of  $2 \times 3$  or  $2 \times 4$  apertures, respectively. In order to save overhead time, we clustered the objects into AORs with the same aperture grid pattern. We used a ramp (exposure) time of 30 s and 12 cycles at each spatial position. This permits up to effectively 720 s (24 cycles) integration time for some spatial positions in the  $1 \times 2$  and  $1 \times 3$  patterns and up to 1080 s (36 cycles) for some positions in the  $2 \times 3$  and  $2 \times 4$  patterns.

Our data were processed and calibrated with version S15.3.0 of the standard IRS pipeline at the *Spitzer* Science Center. We use CUBISM, the CUbe Builder for IRS Spectral Mapping, (version 1.50) to build our post-BCD (basic calibrated data) data products. CUBISM is described in Smith et al. (2007a) and references therein, as well as in a manual detailing its use (Smith et al. 2007b). CUBISM was used to build maps, including accounting for aperture overlaps, and to deal effectively with bad pixels. From the IRS mapping observations, it can combine these data into a single 3-dimensional cube with two spatial and one spectral dimension. For each of our programme H II regions, we constructed a data cube. Global bad pixels (those occurring at the same pixel in every BCD) were removed manually. Record level bad pixels (those occurring only within individual BCDs) that deviated by  $5\sigma$  from the median pixel value and occurred within at least 10 per cent of the BCDs were removed automatically in CUBISM with the “Auto Bad Pixels” function. In reducing our data, we were careful to monitor that the “Auto Bad Pixels” function did not incorrectly flag any of the pixels on our programme spectral lines as bad. Data cubes for each H II region were built without applying the slit-loss correction factors (SLCFs). This is discussed below. We varied our spatial extraction aperture size [always a 2-D integer pixel grid] due to the differences in the size of the observing grid over the particular nebula. Our further analysis of these spectra uses the line-fitting routines in the IRS Spectroscopy Modeling Analysis and Reduction Tool (SMART, Higdon et al. 2004).

The emission lines were measured with SMART using a Gaussian line fit. The continuum baseline was fit with a linear or quadratic function. Figures 2 (a)–(e) show the fits for each of the five lines in BCLMP 45 (object #6 in Fig. 1). A line is deemed to be detected if the flux is at least as large as the  $3\sigma$  uncertainty. We measure the uncertainty by the product of the full-width-half-maximum (FWHM) and the root-mean-square variations in the adjacent, line-free continuum; it does not include systematic effects.

In section 2 of our M83 paper (R07), we discussed and estimated systematic uncertainties as they affected the line fluxes. Here we recap (or repeat) the major points. Most likely the largest uncertainty is due to slit (aperture) loss correction factors (SLCFs). The pipeline flux calibration assumes that objects are point sources. Our nebulae are extended and that is why we mapped each with a grid that covers more than a single aperture. We did not make a correction for this effect. Thus we have implicitly assumed that the H II regions are close to the point-source limit within the SH  $11.3'' \times 4.7''$  aperture. If the H II region were uniformly extended within the SH aperture, SLCFs would need to be applied to our fluxes. These are: 0.697, 0.671, 0.663, 0.601, and 0.543 for the 10.5, 12.4, 12.8, 15.6, and 18.7  $\mu\text{m}$  lines, respectively. These factors were obtained by interpolating in numbers provided from the ‘*b1\_slitloss\_convert.tbl*’ file from the *Spitzer* IRS Custom Extraction tool (SPICE) for the SH module. For the uniformly filled aperture, the maximum uncertainty in the flux due to this effect would be  $\sim$ 46 per cent for the [S III] 18.7 line. The SLCFs would need to multiply our listed fluxes. We note that with regard to this effect, the fluxes listed in Table 2 are upper limits and that the uncertainty would be only in the direction to lower them. No correction factor was applied because we are likely closer to the point-source limit than the uniform-brightness limit. Because our science depends on line flux ratios, for our purposes, the possible uncertainty due to this effect would be lower, e.g.,  $\sim$ 22 per cent when we deal with the line flux ratio [S IV] 10.5/[S III] 18.7. The possible uncertainty in the absolute flux calibration of the spectroscopic products delivered by the pipeline is likely confined to between  $\pm$ 5 per cent and  $\pm$ 10 per cent. Any uncertainty in the flux due to a pointing error is probably small and in the worst case should not exceed 10 per cent.

For the brighter lines, that is, most of the 10.5, 12.8, 15.6, and 18.7  $\mu\text{m}$  lines, the systematic uncertainty far exceeds the measured (statistical) uncertainty. Even for the fainter lines, we estimate that the systematic uncertainty exceeds the measured uncertainty. In addition to the line flux, the measured FWHM and heliocentric radial velocities ( $V_{\text{helio}}$ ) are listed in Table 2. Both the FWHM and  $V_{\text{helio}}$  are useful in judging the reliability of the line measurements. The FWHM is expected to be the instrumental width for all our lines. With a resolving power for the SH module of  $\sim$ 600, our lines should have a FWHM of roughly 500  $\text{km s}^{-1}$ . The values for  $V_{\text{helio}}$  should straddle the heliocentric systemic radial velocity for M33 of  $-179 \text{ km s}^{-1}$  (Corbelli & Schneider 1997). Most of our measurements are in agreement with these expectations.

### 3. Variation in the degree of ionization of the H II regions with $R_G$

We chose our sample of nebulae in order to cover a wide range in  $R_G$  (in the plane of M33). To derive these deprojected galactocentric distances, we used a distance D of 840 kpc (Freedman, Wilson, & Madore 1991) an inclination angle ( $i = 56 \pm 1^\circ$ ), and a position angle of the line of nodes ( $\theta = 23 \pm 1^\circ$ ) (Zaritsky, Elston, & Hill 1989). We assumed the centre of the galaxy is at  $\alpha, \delta = 1^{\text{h}}33^{\text{m}}51\overset{\text{s}}{.}02, 30^\circ39'36\overset{\text{s}}{.}7$  (J2000) (Cotton, Condon, & Arbizzani 1999). Table 3 lists  $R_G$  for the centre of each object. These range from from 0.71 to 6.73 kpc.

From the measured fluxes, we estimate ionic abundance ratios, including  $\text{Ne}^{++}/\text{Ne}^+$ ,  $\text{S}^{3+}/\text{S}^{++}$ , and  $\text{S}^{++}/\text{Ne}^+$ , for each of the H II regions. Important advantages compared with prior optical studies of various other ionic ratios are: (1) the IR lines have a weak and similar electron temperature ( $T_e$ ) dependence while the collisionally-excited optical lines vary exponentially with  $T_e$ , and (2) the IR lines suffer far less from interstellar extinction. Indeed for our purposes, the differential extinction correction is negligible as the lines are relatively close in wavelength. In our analysis, we deal with ionic abundance ratios and therefore line flux ratios. In order to derive the ionic abundance ratios, we perform the usual semiempirical analysis assuming a constant  $T_e$  and electron density ( $N_e$ ) to obtain the volume emissivities for the five pertinent transitions. For the ions  $\text{Ne}^+$ ,  $\text{Ne}^{++}$ ,  $\text{S}^{++}$ , and  $\text{S}^{3+}$ , we use the atomic data described in Simpson et al. (2004) and Simpson et al. (2007). For  $\text{H}^+$  from the H(7–6) line, we use Storey & Hummer (1995). There is a bit of a complication here because at Spitzer’s spectral resolution, the H(7–6) line is blended with the H(11–8) line. Their respective  $\lambda(\text{vac}) = 12.371898$  and  $12.387168 \mu\text{m}$ . In order to correct for the contribution of the H(11–8) line, we use the relative intensity of H(11–8)/H(7–6) from recombination theory (Storey & Hummer 1995) assuming case B and  $N_e = 100 \text{ cm}^{-3}$ . The ratio  $\text{H}(11-8)/\text{H}(7-6) = 0.122$  and holds over a fairly wide range in  $N_e$  and  $T_e$  [including 8000 and 10000 K, see below] appropriate for our objects, and indeed for case A also.

For the entries in Table 3, we adopt a value for all the M33 H II regions of  $T_e = 8000 \text{ K}$  and  $N_e = 100 \text{ cm}^{-3}$ . In a recent paper, Magrini et al. (2007) were able to derive  $T_e$  for 14 H II regions in M33 from the diagnostic flux ratio  $[\text{O III}] 4363/(5007 + 4959)$ . Only one of their objects BCLMP 45 can be clearly identified with one of our regions. They found  $T_e[\text{O III}] = 8600 \pm 200 \text{ K}$ . Furthermore, this object was one of only three where they also determined  $T_e[\text{N II}]$  from the flux ratio  $5755/(6584 + 6548)$ ; the result was  $8200 \pm 1000 \text{ K}$ . There are two more of our programme sources with available  $T_e[\text{O III}]$ . These were derived by Crockett et al. (2006) from their optical observations of BCLMP 691 yielding  $10000 \pm 200 \text{ K}$  and recomputing  $T_e$  with the measurements for BCLMP 280 (NGC 588) from Vílchez et al. (1988) resulting in  $9300^{+600}_{-400}$ . While these values for  $T_e$  are somewhat higher than the 8000 K we adopt, we point out a well-known bias. That is, both  $T_e[\text{O III}]$  and  $T_e[\text{N II}]$  derived from

the ratio of fluxes of “auroral” to “nebular” lines are systematically higher than the so-called “ $T_0$ ”, which is the  $(N_e \times N_i \times T_e)$ -weighted average, where  $N_i$  is the ion density of interest. The amount of this bias depends on the degree of  $T_e$  variations in the observed volume (see Peimbert 1967 and many forward references). In our analysis, using the set of IR lines, it is more appropriate to be using a  $T_e$  that is similar to  $T_0$ . Because of the insensitivity of the volume emissivities to  $T_e$ , particularly when working with ratios for these IR lines, our results depend very little on this  $T_e$  choice. The effects on our analysis due to a change in the assumed  $N_e$  are also small as will be discussed later.

We present the variation of  $\text{Ne}^{++}/\text{Ne}^+$  with  $R_G$  in Figure 3 using the values from Table 3. The error values here, as well as for all others in Table 3 and in Figures 4–8, represent the propagated flux measurement uncertainties and *do not include the systematic uncertainties*. Our assumed  $N_e$  of  $100 \text{ cm}^{-3}$  appears reasonable in view of previous observations that address the density. For instance, Magrini et al. (2007) derived  $N_e$  from the familiar diagnostic line flux ratio [S II] 6717/6731. For most of their H II regions, they found that this ratio was consistent with the low- $N_e$  asymptotic limit, that is,  $N_e < 100 \text{ cm}^{-3}$ . There is extremely little change in any of our derived  $\text{Ne}^{++}/\text{Ne}^+$  ratios even when using an  $N_e$  of  $1000 \text{ cm}^{-3}$ , which is likely an upper limit for these H II regions. A linear least-squares fit indicates a positive correlation with  $R_G$  (in kpc),

$$\text{Ne}^{++}/\text{Ne}^+ = -0.44 \pm 0.22 + (0.46 \pm 0.067) R_G,$$

with minuscule change to this equation for  $N_e = 1000 \text{ cm}^{-3}$ . For all the least-squares line fits in this paper, each point is given equal weight because systematic uncertainties exceed the flux measurement uncertainties, as discussed earlier. The positive correlation of  $\text{Ne}^{++}/\text{Ne}^+$  with  $R_G$  as measured by the slope may be judged to be significant following the criterion that it exceeds the  $3\sigma$  uncertainty. We also did a linear least-squares fit to  $\log(\text{Ne}^{++}/\text{Ne}^+)$  vs.  $R_G$  with the result

$$\log(\text{Ne}^{++}/\text{Ne}^+) = -0.88 \pm 0.11 + (0.20 \pm 0.035) R_G.$$

This relation also produces a statistically significant slope. The transformation of this function is shown as the dashed line in Figure 3. Three objects (230, 702, and 740W) have been excluded in this Figure as well as in Figure 4 because of poor S/N and/or extreme deviancy from the trend of the 22 other sources. The slope in the linear plot here  $0.46 \pm 0.067$  is much steeper than the analogous slope for our M83 H II regions of  $0.011 \pm 0.0035$  (see Figure 3 in R07). Furthermore, the comparison with Figure 3 in the M83 paper shows dramatically the higher ionization of the M33 nebulae.

A similar fit to the  $\text{S}^{3+}/\text{S}^{++}$  vs.  $R_G$  data yields

$$S^{3+}/S^{++} = -0.032 \pm 0.018 + (0.046 \pm 0.0057) R_G.$$

The slope exceeds the  $1\sigma$  uncertainty by a factor of 8. Thus the increase in degree of ionization with increasing  $R_G$  here too is significant. A linear least-squares fit to  $\log(S^{3+}/S^{++})$  vs.  $R_G$  results in

$$\log(S^{3+}/S^{++}) = -1.7 \pm 0.090 + (0.18 \pm 0.028) R_G.$$

Again there is a statistically significant slope. We map this relation onto Figure 3 as the dashed line. While there is no fundamental reason to expect either functional form shown in Figures 3 and 4, we note that the dashed line fits do have the advantage of not extrapolating to negative ionic ratios at small values of  $R_G$ .

Figure 5 plots the fractional ionic abundance ratio  $\langle S^{++} \rangle / \langle Ne^+ \rangle$  vs.  $R_G$  for 23 H II regions (sources 230 and 702 are excluded). This ratio is obtained from the  $S^{++}/Ne^+$  ratio by multiplying by an assumed  $Ne/S$  value (see below). The last three columns of Table 3 list this and other fractional ionic abundance ratios used in this paper. We show the linear least-squares fit for an assumed  $N_e$  of  $100 \text{ cm}^{-3}$ . Here, the fit indicates a significant positive correlation with  $R_G$ ,

$$\langle S^{++} \rangle / \langle Ne^+ \rangle = 0.56 \pm 0.23 + (0.31 \pm 0.069) R_G,$$

where angular brackets denote fractional ionization. In this figure and in the linear fit, we assume an Orion Nebula  $Ne/S$  abundance ratio of 14.3 (Simpson et al. 2004). Because  $Ne$  and  $S$  are “primary” elements, their production is expected to vary in lockstep and  $Ne/S$  would not be expected to show a radial gradient within a galaxy (Pagel & Edmunds 1981). There is a clear correlation of increasingly higher ionization with increasing  $R_G$ . One reason may be due to the lower metallicity at larger  $R_G$  (see section 5) causing the exciting stars to have a harder ionizing spectrum.

#### 4. Neon to Sulfur abundance ratio

For H II regions, we may approximate the  $Ne/S$  ratio with  $(Ne^+ + Ne^{++})/(S^{++} + S^{3+})$ . This includes the dominant ionization states of these two elements. However this relation does not account for  $S^+$ , which should be present at some level. We may safely ignore the negligible contributions of neutral  $Ne$  and  $S$  in the ionized region. Figure 6 shows our approximation for  $Ne/S$  vs.  $R_G$ . The linear least-squares fit to 23 objects (again omitting for cause sources 230 and 702) is

$$Ne/S = 18.0 \pm 1.3 - (0.39 \pm 0.40) R_G,$$

plotted as the dotted line in Figure 6. We also show the fit, the solid line, after removing the remaining deviant large value (source 32). The relation becomes

$$\text{Ne/S} = 16.8 \pm 0.97 - (0.14 \pm 0.29) R_G.$$

Both of these indicate that there is no significant slope. Our data also indicate that the lower envelope to Ne/S is well fit by a constant value equal to the Orion Nebula ratio of 14.3 (Simpson et al. 2004).

In our previous M83 results, there appeared to be a drop in the Ne/S ratio with increasing  $R_G$ . We argued that this was not a true gradient in Ne/S. Instead, it is most likely due to not accounting for the presence of sulfur in other forms –  $S^+$ , molecules, and dust. Because our observations of the H II regions in M83 showed an increasing degree of ionization with increasing  $R_G$ , the expected increasing fraction of  $S^+$  towards the inner galaxy regions would lead to a flatter gradient. Another factor that could flatten the slope is the higher dust content (with S, but not Ne, entering grains) expected in the inner regions due to higher metallicity as is the case for the Milky Way. The refractory carbonaceous and silicate grains are not distributed uniformly throughout the Galaxy but instead increase in density toward the centre. A simple model suggests the dust density is  $\sim 5 - 35$  times higher in the inner parts of the Galaxy than in the local ISM (Sandford, Pendleton, & Allamandola 1995). The Ne/S abundance ratios that we derived for 24 H II regions in M83 varied from 41.9 to 24.4 (see Figure 5 in R07). All are considerably higher than the Orion Nebula value of 14.3 and, as an ensemble, significantly higher than what we find here for the nebulae in M33. Thus the evidence is strong that the derived Ne/S estimates for the M83 objects are upper limits and furthermore, those that are further from the centre will likely need less of a downward correction to obtain a true Ne/S ratio.

Because the M33 H II regions have a lower metallicity and because almost all have a significantly higher ionization than those we observed in M83, the amount of any correction needed for S in forms other than  $S^{++}$  and  $S^{3+}$  is minimized. Hence while our derived Ne/S ratios should still be considered as upper limits, these M33 values are a much more robust estimate of a true Ne/S ratio than those for M83. The scenario above is in excellent accord with the recent results of Wu et al. (2008), hereafter W08. They obtained an average  $\text{Ne/S} = 12.5 \pm 3.1$  from *Spitzer* observations of 13 blue compact dwarf galaxies and found no correlation between their Ne/S and Ne/H ratios. The median (average) Ne/S ratio derived for 23 H II regions in M33 is 16.3 (16.9).

## 5. Variation in the Ne/H and S/H ratios with $R_G$

There was a significant detection of the H(7-6) flux for 16 of the H II regions (see Table 2) which permits a determination of the heavy element abundances Ne/H and S/H (see Table 3). We present the results for Ne/H in Figure 7. A linear least-squares fit of  $\log(\text{Ne}/\text{H})$  vs.  $R_G$  results in

$$\log(\text{Ne}/\text{H}) = -4.07 \pm 0.04 - (0.058 \pm 0.014) R_G.$$

This fit indicates a significant slope ( $4.1 \sigma$ ). A similar plot for S/H is shown in Figure 8. Here the linear least-squares fit to  $\log(\text{S}/\text{H})$  vs.  $R_G$  yields

$$\log(\text{S}/\text{H}) = -5.31 \pm 0.06 - (0.052 \pm 0.021) R_G.$$

It is interesting that the slope is nearly identical to the Ne/H relationship. However, the slope signal-to-noise ratio ( $2.5 \sigma$ ) is less than  $3 \sigma$  and thus would be deemed only marginally significant. While *Spitzer* is an admirable machine for measuring both Ne and S abundances in H II regions, the neon abundances are determined more reliably. As previously mentioned, with the *Spitzer* observations alone, we are neither accounting for  $\text{S}^+$  nor S that may be tied up in dust or molecules. In this sense, the S/H ratios in Figure 8 are lower limits. Both of the above measurements of a heavy element abundance gradient are in remarkable agreement with the recent value for the  $\log(\text{O}/\text{H})$  gradient of  $-0.054 \pm 0.011 \text{ dex kpc}^{-1}$  (Magrini et al. 2007). They derived this gradient from optical observations of 14 H II regions in M33 where the [O III] (5007, 4959, 4363 Å) and [O II] (7320, 7330 Å) emission line fluxes were all measured and a value for  $T_e$  determined. The sources for their linear least-squares fit covered a range in  $R_G$  from  $\sim 2$  to  $7.2 \text{ kpc}$  and resulted in  $\log(\text{O}/\text{H}) = -3.47 \pm 0.05 - (0.054 \pm 0.011) R_G$ . Because the slope for this is practically the same as ours above for  $\log(\text{Ne}/\text{H})$ , we may use the respective y-intercepts to infer a Ne/O ratio of 0.28. This is in good agreement with the  $\text{Ne}/\text{O} = 0.25$  value for the Orion Nebula (Simpson et al. 2004). Using *ISO*, Willner & Nelson-Patel (2002) measured the neon lines in M33. If the two outermost objects in their sample are neglected, they found a neon gradient of  $-0.05 \pm 0.02 \text{ dex kpc}^{-1}$ , which agrees with the slope we find.

## 6. Constraints on the ionizing SED for the stars exciting the H II regions

Various fractional ionic abundances are highly sensitive to the stellar ionizing SED that apply to H II regions. The present *Spitzer* data probe the  $\text{Ne}^+$  and  $\text{Ne}^{++}$  fractional ionic abundances, as well as those of  $\text{S}^{++}$  and  $\text{S}^{3+}$ . They may be used to provide further constraints and tests on the ionizing SED for the stars exciting these M33 nebulae, similar to

what we had done in the M83 paper (R07). We use the ratio of fractional ionizations  $\langle \text{Ne}^{++} \rangle / \langle \text{S}^{++} \rangle$  vs.  $\langle \text{S}^{3+} \rangle / \langle \text{S}^{++} \rangle$  (Figure 9a),  $\langle \text{Ne}^{++} \rangle / \langle \text{S}^{3+} \rangle$  vs.  $\langle \text{S}^{3+} \rangle / \langle \text{S}^{++} \rangle$  (Figure 9b), and  $\text{Ne}^{++}/\text{Ne}^+$  vs.  $\langle \text{S}^{3+} \rangle / \langle \text{S}^{++} \rangle$  (Figure 9c). These ionic ratios are computed using our photoionization code NEBULA (e.g., Simpson et al. 2004; Rodríguez & Rubin 2005). The lines connect the results of the nebular models calculated using the ionizing SEDs predicted from various stellar atmosphere models. There are no other changes to the input parameters, just the SED. The stellar atmospheres used are representative of several non-LTE models that apply for O-stars. We also display the results from one set of LTE models (Kurucz 1992). His LTE atmospheres have been extensively used in the past as input for H II region models. Hence the comparison with the other non-LTE results reinforces the fact that more reliable SEDs for O-stars require a non-LTE treatment. Figures 9a–c dramatically illustrate how sensitive H II region model predictions of these ionic abundance ratios are to the ionizing SED input to nebular plasma simulations.

We list for each model the ( $T_{\text{eff}}$  in kK,  $\log g$ )-pair to identify it. There are other parameters for a stellar atmosphere model such as the elemental abundance mix and those that describe stellar winds, which are treated in each of these non-LTE codes. Basically, all the atmospheres use solar abundances. For the H II region models calculated with Pauldrach et al. (2001) atmospheres, the solid line connects models with “dwarf” atmospheres and the dashed line connects models with “supergiant” atmospheres. Proceeding from the hot to the cool end, the Pauldrach et al. dwarf set has (50, 4), (45, 3.9), (40, 3.75), (35, 3.8), and (30, 3.85) while the supergiant set has (50, 3.9), (45, 3.8), (40, 3.6), (35, 3.3), and (30, 3). In several instances, the loci are cut off at the edges of the plot at the cool end as they track toward the point computed with the coolest atmosphere. The Sternberg et al. (2003) paper also uses Pauldrach’s WM-BASIC code. At a given  $T_{\text{eff}}$  we have used their model with the smallest  $\log g$  in order to be closest to the supergiant case. Because the locus using these Sternberg et al. atmosphere models is for the most part similar to the Pauldrach et al. supergiant locus, we do not show it in Figures 9 to avoid clutter.

The violet lines with inverted triangles are for H II region models calculated with Lanz & Hubeny (2003) atmospheres (TLUSTY code). The solid line connects models using atmospheres with (45, 4), (40, 4), (35, 4), and (30, 4) while the dotted line connects models using atmospheres with (45, 3.75), (40, 3.5), (37.5, 3.5), (35, 3.25), (32.5, 3.25), and (30, 3). The orange squares are the results of our nebular models with the atmospheres in Martins et al. (2005) that use Hillier’s CMFGEN code. The dotted line connects models using atmospheres with (48.53, 4.01), (42.56, 3.71), (40, 3.5), (37.5, 3.5), (35, 3.25), (35, 3.5), and (32.5, 3.5). The brown line with triangles result from the models using Kurucz (1992) atmospheres with (45, 4.5), (40, 4.5), (37, 4), (35, 4), and (33, 4).

To compare our data with the models in Figures 9a,b, we need to divide the observed  $\text{Ne}^{++}/\text{S}^{++}$  and  $\text{Ne}^{++}/\text{S}^{3+}$  ratios by an assumed Ne/S abundance ratio. For this purpose, we adopt a constant  $\text{Ne}/\text{S} = 14.3$ , the Orion Nebula value (Simpson et al. 2004). The open red circles are our prior results for the M83 H II regions. The green stars are the M33 results (adjusted by the assumed Ne/S) derived from our observed line fluxes using  $N_e$  of  $100 \text{ cm}^{-3}$ . While the  $\langle \text{Ne}^{++} \rangle / \langle \text{Ne}^+ \rangle$  ratio in Figure 9c has the advantage of being independent of elemental abundance ratios, it appears to be more sensitive to the *nebular* parameters than the others, as will be discussed later. The trends of the ionic ratios established from the prior M83 study are remarkably similar, but continued to higher ionization with the present M33 objects. There are two sources, one in M33 and one in M83, that are deviantly low compared with the theoretical tracks and the other data. The point that is low in all three panels for M33 is BCLMP 702, which is the faintest of the M33 regions in the 10.5 and  $12.8 \mu\text{m}$  lines. Also the FWHM of  $903 \text{ km s}^{-1}$  measured for the  $15.6 \mu\text{m}$  line is the largest (see Table 2) and possibly suspect. The deviant object in M83 (in all three panels) is source RK 268, which is the faintest of the M83 regions in the  $12.8$ ,  $15.6$ , and  $18.7 \mu\text{m}$  lines. For the  $10.5 \mu\text{m}$  line, it is the second broadest line, FWHM of  $809 \text{ km s}^{-1}$ , of any line we measured in M83 (see Table 2 in R07). Thus we consider the position of both of these sources to be duly suspect in Figures 9. On the whole, the data for both galaxies in panels a and b lie closest to the theoretical loci obtained with the Pauldrach et al. supergiant SEDs. This is particularly notable in Figure 9b, where the other model loci are nearly perpendicular to the data point trend in the vicinity of where they intersect the data points. On the other hand, the data in panel c, for the most part, appear to lie closer to Martins et al., Lanz & Hubeny et al., and Pauldrach et al. *dwarf* loci.

The nebular models used to generate Figures 9 are all constant density, ionization-bounded, spherical models. We used a constant total nucleon density (DENS) of  $1000 \text{ cm}^{-3}$  that begins at the star. Each model used a total number of Lyman continuum photons  $\text{s}^{-1}$  ( $N_{LyC}$ ) =  $10^{49}$ . The same *nebular* elemental abundance set was used for all nebular models. We use the same “reference” set as in Simpson et al. (2004) because in that paper we were studying the effects of various SEDs on other ionic ratios and other data sets. Ten elements are included with their abundance by number relative to H as follows: (He, C, N, O, Ne, Si, S, Ar, Fe) with (0.100,  $3.75\text{E}-4$ ,  $1.02\text{E}-4$ ,  $6.00\text{E}-4$ ,  $1.50\text{E}-4$ ,  $2.25\text{E}-5$ ,  $1.05\text{E}-5$ ,  $3.75\text{E}-6$ ,  $4.05\text{E}-6$ ), respectively. We continue with the same set of abundances as in the M83 paper (R07). As we mentioned there, the set of abundances used is roughly a factor of 1.5 higher than for Orion and not drastically different from solar. These heavy element abundances are too high for M33 and we investigate below how the theoretical loci will change when these abundances are scaled back accordingly.

We have investigated the effects of changing DENS,  $N_{LyC}$ , and allowing for a central

evacuated cavity, characterized by an initial radius ( $R_{init}$ ) before the stellar radiation encounters nebular material. We term these shell models. In Figures 10a–c, the resulting changes to Figures 9a–c are shown for 12 nebular models run using the Pauldrach et al. (2001) supergiant atmospheres with  $T_{eff}$  35, 40, and 45 kK. These models are listed along with the symbol in Table 4. The original Pauldrach et al. (2001) supergiant locus (the dashed line connecting the filled circles) and points derived from the *Spitzer* M33 and M83 data are shown again.

The points for models 3, 7, and 11 are nearly identical to the original points for the Pauldrach supergiant models at the same respective  $T_{eff}$ . This can be understood in terms of the ionization parameter ( $U$ ), which is very useful for gauging ionization structure. An increase in  $U$  corresponds to higher ionization (for a given  $T_{eff}$ ). For an ionization-bounded, constant density case,

$$U = [N_e N_{LyC} (\alpha - \alpha_1)^2 / (36\pi c^3)]^{1/3},$$

where  $(\alpha - \alpha_1)$  is the recombination rate coefficient to excited levels of hydrogen, and  $c$  is the velocity of light (see Rubin et al. 1994, eq. 1 and adjoining discussion). Because  $(\alpha - \alpha_1) \simeq 4.10 \times 10^{-10} T_e^{-0.8} \text{ cm}^3 \text{ s}^{-1}$  (Rubin 1968 fit to Seaton 1959), there is only a weak dependence of  $U$  on  $T_e$  ( $\sim T_e^{-0.5}$ ). When  $U$  is similar, as is the case here with the product of  $N_e \times N_{LyC}$ , the ionization structure is similar. With regard to the three shell models in Figures 10, the Strömgren radius is  $\sim 0.74$  pc. Thus the radial thickness of the shell is slightly less than half the radius of the central cavity. From the visual appearance of our target H II regions, it is unlikely that the theoretical loci need to be tracked to higher dilutions.

Another *nebular* parameter that can alter the theoretical tracks is the set of elemental abundances used. To investigate this effect and to have a set more representative of the lower metallicity of M33, we have calculated three models (numbers 4, 8, and 12 in Table 4) reducing all the heavy element abundances by a factor of three from the “reference” set. As expected, lower metallicity results in a shift to higher ionization. In Figures 10a,b,c the point moves to the upper right. For  $T_{eff}$  35kK, the factors are  $\langle \text{Ne}^{++} \rangle / \langle \text{S}^{++} \rangle = 1.85$ ,  $\langle \text{Ne}^{++} \rangle / \langle \text{S}^{3+} \rangle = 1.44$ ,  $\langle \text{S}^{3+} \rangle / \langle \text{S}^{++} \rangle = 1.29$ , and  $\langle \text{Ne}^{++} \rangle / \langle \text{Ne}^+ \rangle = 1.91$ . For  $T_{eff}$  40kK, the respective factors are 1.39, 1.23, 1.14, and 1.65. For  $T_{eff}$  45kK, the respective factors are 1.14, 1.10, 1.03, and 1.45. Likewise, higher metallicity shifts the point to the lower left (R07). The above factors show that there is a progression to a smaller influence on these ionic ratios with metallicity as  $T_{eff}$  increases from 35 to 45kK. Additionally, the largest change is always in the  $\langle \text{Ne}^{++} \rangle / \langle \text{Ne}^+ \rangle$  ratio and the smallest is in the  $\langle \text{S}^{3+} \rangle / \langle \text{S}^{++} \rangle$  ratio. While the  $\langle \text{Ne}^{++} \rangle / \langle \text{Ne}^+ \rangle$  ratio has the advantage of being independent of elemental abundance ratios, it appears to be more sensitive to the *nebular* parameters than does the other ratios. Note that the y-axis scales are different in Figures 10 a, b, and c and thus a simple visual guide from the length of the various line segments cannot be used as an

accurate measure of the effect of changing a nebular parameter between the three panels. It is interesting that there appears to be a small, upward shift of the M33 star points with respect to the trend of the M83 points (circles), particularly noticeable in Fig. 10c (and in the electronic colour version). This is qualitatively what is expected for the lower metallicity H II regions of M33. The dashed line theoretical locus would move up, connecting the square points. Nevertheless, for both the case of the M33 and M83 nebulae, we may conclude that the predicted spread in Figures 10 due to a reasonable uncertainty in nebular metallicity is far less than that due to the SEDs of the various stellar atmosphere models.

The magnitude/direction of changes in Figures 10 due to varying the *nebular* parameters per Table 4 should be roughly similar for the other models shown in Figures 9. It is also noted that we have not considered matter-bounded nebular models. These would be higher ionization than the corresponding ionization-bounded model. There is also the effect of a change in the abundances used to compute the stellar atmosphere models. This will change the emergent stellar SED (e.g., Mokiem et al. 2004). As is the case for a change in the nebular model abundance set, such a modification in the stellar model will alter the shape of the SED in the same sense; that is, a higher metallicity will cause more opacity and soften the SED, and a lower metallicity will do the opposite. Mokiem et al. (2004) examined this using CMFGEN stellar models matching both the nebular and stellar metallicities. Their Figure 11 tracks the predicted variation in the [Ne III] 15.6/[Ne II] 12.8 flux ratio over a range of  $0.1 - 2 Z_{\odot}$ . Although beyond the scope of this paper, it would be interesting to compare models using different stellar atmosphere metallicities, especially if the environment indicates significant departures from solar. However, the proper abundances are not accurately known and comparisons like those in this paper will help decipher the proper values. With the present paper, however, we have been investigating which of the models best fits the observations and such a comparison works most effectively with a fixed set of abundances *common to all models*, which are the solar ones.

There appears to be a remarkable “convergence” of the nebular models close to the hot (right) side of Figures 9. Depending on the set of stellar atmosphere models, there is a significant spread in  $T_{\text{eff}}$  ( $\sim 42\text{--}50\text{kK}$ ) (as well as the  $\log g$  parameter) in the vicinity where this occurs. For instance, the results in all three panels are essentially identical using either the TLUSTY (45, 3.75) or the WM-BASIC (50, 3.9) SED. A likely explanation for this convergence behaviour in Figures 9 is that at these high  $T_{\text{eff}}$  values, the ionization balance in the atmospheres shifts to higher ionization stages which have fewer lines that can influence the model calculations. Thus, blocking and blanketing effects no longer dominate the models as strongly, and the line radiation pressure is also less significant. This means that the influence of the expanding atmosphere decreases. As a result of all this, at high  $T_{\text{eff}}$  the model calculation are no longer as critically dependent on the correct treatment of the

complex details of the physics involved.

## 7. Discussion

With the recent papers by W08 and Lebouteiller et al. (2008), hereafter L08, we are in a position to further examine the Ne/S ratio discussed in §4. Fundamental observational data are vital to test and constrain theories of nucleosynthesis and GCE. A very valuable adjunct would be to find how much the Ne/S ratio can vary or whether or not there is a fairly “universal” value. W08 obtained an average  $\text{Ne}/\text{S} = 12.5 \pm 3.1$  from *Spitzer* observations of 13 blue compact dwarf galaxies. They found no correlation between their Ne/S ratios with metallicity (the Ne/H ratios). With their Table 3 of line fluxes, we apply the same methods used here for the M33 objects to derive the various ionic abundance ratios. For the same blue compact dwarf galaxy, we obtain somewhat higher Ne/S ratios. We are particularly interested in combining their observations with ours to address the Ne/S ratio and whether there is any correlation with degree of ionization as measured by the  $\text{Ne}^{++}/\text{Ne}^+$  and  $\text{S}^{3+}/\text{S}^{++}$  ratios. Nine of the galaxies in W08 had all four of the necessary lines detected to derive both of these ratios (i.e., we excluded their 4 objects which had at least one upper limit on a line flux). In Table 5, we list in columns 2–4,  $\text{Ne}^{++}/\text{Ne}^+$ ,  $\text{S}^{3+}/\text{S}^{++}$ , and Ne/S derived by us using the individual  $T_e$ – and  $N_e$ –values in Wu et al.’s Table 2. In columns 5–7, we list the same set derived here assuming  $T_e = 10000$  K and  $N_e = 100 \text{ cm}^{-3}$ . It is apparent that there is very little difference between these due to what ( $T_e$ ,  $N_e$ ) values are used. The median (average) Ne/S for the 9 galaxies in column 4 is 14.0 (14.9), while it is 13.9 (14.9) from column 7. However, for these 9 objects, the median Ne/S is 12.4 and the average 12.7 (from Table 4 in W08).

L08 reported their Spitzer observations of three very massive H II region: the Galactic source NGC 3603; the extremely massive 30 Dor in the Large Magellanic Cloud; and N 66 (NGC 346), the largest in the Small Magellanic Cloud. With their Table 2 of line fluxes, we apply the same methods used here for the M33 objects to derive the various ionic abundance ratios. In their Table 6, they list derived abundance ratios for several position observed in each object: 3 for NGC 3603, 15 for 30 Dor, and 11 for N 66. Again, we find somewhat higher Ne/S ratios at all positions than the corresponding value obtained from their Table 6. In Table 6 here, we list in columns 2–4,  $\text{Ne}^{++}/\text{Ne}^+$ ,  $\text{S}^{3+}/\text{S}^{++}$ , and Ne/S derived by us using the same  $T_e$ – and  $N_e$ –values as they had used. These are 10000 K and  $1000 \text{ cm}^{-3}$  for NGC 3603; 10000 K and  $100 \text{ cm}^{-3}$  for 30 Dor; and 12500 K and  $100 \text{ cm}^{-3}$  for N 66. The median Ne/S ratios we derive for NGC 3603, 30 Dor, and N 66. are 14.6, 11.4, and 10.1, respectively.

Some variation is traceable to the adoption of different [S III] effective collision strengths.

We use the set by Tayal & Gupta (1999); W08 and L08 stated that they used values from the IRON Project, which for this ion would be “paper X” (Galavís et al. 1995). There is a substantial difference between the values in these papers. For instance the values between the ground-state, fine structure levels (where the [S III] IR lines arise) at  $T_e = 10000$  K are: 3.98, 1.31, and 7.87 (Tayal & Gupta) and 2.331, 1.110, and 5.411 (Galavís et al.) for transitions  $^3P_0 - ^3P_1$ ,  $^3P_0 - ^3P_2$ , and  $^3P_1 - ^3P_2$  respectively. Furthermore, these three values show a change in *opposite directions* with  $T_e$  decreasing from 10000 K. The above three collision strengths increase in the Tayal & Gupta work but decrease in the other study. In H II regions, S<sup>++</sup> is almost always more abundant than S<sup>3+</sup> as is the case for every point here except 1 of the 9 W08 galaxies addressed here. Because we use the larger [S III] effective collision strengths, the S<sup>++</sup> abundance we infer will be lower than what was derived in the other two papers. This will then result in the total S abundance ( $S^{++} + S^{3+}$ ) being smaller and hence the Ne/S abundance larger than what W08 and L08 found. Following Simpson et al. (2007), we repeat here the references for the other effective collision strengths we use: [S IV] (Sarah & Storey 1999), [Ne II] (Sarah & Tully 1994), and [Ne III] (McLaughlin & Bell 2000). Apparently W08 and L08 did use the same sets for [Ne II] and [S IV] but probably used “paper V” (Butler & Zeippen 1994) from the IRON Project for [Ne III]. We note that near  $T_e = 10000$  K, the values for [Ne III] are quite similar. Even without passing judgment on the relative merits of one set of effective collision strengths vs. another, it is crucial for the purposes of this paper that we continue the analysis with a homogeneous treatment. For this we will use the adjusted ionic ratios from columns 2–4 in Tables 5 and 6.

In Figure 11, we plot Ne/S vs. Ne<sup>++</sup>/Ne<sup>+</sup> for our M33 results (star symbol) using the same 22 sources mentioned in Fig. 6. The linear least-squares fit to the M33 points is,

$$Ne/S = 17.02 \pm 0.63 - (0.78 \pm 0.50) Ne^{++}/Ne^+,$$

which is shown as the solid line. The negative gradient is not statistically significant. The results from our prior M83 study (R07) are shown as circles. The wide spread in the M83 points dramatically demonstrates the limitations of our method to infer Ne/S [except as an upper limit] when Ne<sup>++</sup>/Ne<sup>+</sup> is low (i.e., for low ionization objects). The squares show the W08 data for the 9 blue compact dwarf galaxies, as discussed above. The linear least-squares fit to those 9 points is,

$$Ne/S = 18.17 \pm 1.07 - (0.93 \pm 0.24) Ne^{++}/Ne^+.$$

While our M33 data indicate no statistically significant slope, the fit to the 9 blue compact dwarf galaxies shows a statistically significant decrease with higher Ne<sup>++</sup>/Ne<sup>+</sup> (the dotted line in Fig. 11). We note that the median (average) Ne/S for the 9 galaxies is 14.0 (14.9), very close to the Orion value of 14.3 shown as the dashed line. If we exclude the four lowest

ionization galaxies and fit just the five with the highest ionization, then

$$\text{Ne/S} = 15.09 \pm 1.15 - (0.49 \pm 0.20) \text{ Ne}^{++}/\text{Ne}^+,$$

and this flatter negative slope ( $2.5 \sigma$ ) is no longer statistically significant.

In Fig. 11, we also show the reanalyzed results of L08 (see Table 6). There appears to be a trend with the three positions in NGC 3603 (red asterisks) having the highest median Ne/S, followed by the 15 positions in 30 Dor (green triangles), and the 9 positions in N 66 (blue diamonds) having the lowest median ratio. This trend is correlated with the metallicity with NGC 3603 approximately solar, 30 Dor  $\sim 0.7$  solar, and N 66  $\sim 0.2$  solar (L08 and references therein). No error bars are shown on these points, but they may be expected to be roughly 20 percent according to L08. A picture that is consistent with the data in Figure 11 is that at the lowest ionizations there remains considerable S still present at these positions in the form of  $\text{S}^+$ , molecular gas, and dust. The three 30 Dor positions with the lowest ionization, as measured by both  $\text{Ne}^{++}/\text{Ne}^+$  and  $\text{S}^{3+}/\text{S}^{++}$ , are #10 and 17, followed by #8 in Table 6. An inspection of Fig. 2 in L08 shows that positions #10 and 17 are near the periphery of their 30 Dor image and thus might be expected to be characterized by lower ionization than interior positions. The linear least-squares fit to the data in Table 6 excludes these three lowest ionization 30 Dor points as well as the NGC 3603 points. The dash-dot line fits 23 positions, those in N 66 and the 12 remaining in 30 Dor, with the highest ionization. We find,

$$\text{Ne/S} = 12.08 \pm 0.41 - (0.37 \pm 0.12) \text{ Ne}^{++}/\text{Ne}^+,$$

with a slope that is marginally significant ( $3.1 \sigma$ ). We note that there is no basis to extrapolate the line to the edges of the graph as shown, and indeed no theoretical basis for a straight line. What we would expect once all other S species become negligible with respect to  $\text{S}^{++}$  and  $\text{S}^{3+}$  is that an asymptotic Ne/S will be approached at the higher ionizations.

Similar fits to Ne/S vs.  $\text{S}^{3+}/\text{S}^{++}$  are shown in Fig 12 and result in,

$$\text{Ne/S} = 16.67 \pm 0.71 - (3.11 \pm 5.41) \text{ S}^{3+}/\text{S}^{++},$$

for 22 sources in M33. The slope is not significant statistically. For the 9 blue compact dwarf galaxies,

$$\text{Ne/S} = 17.70 \pm 1.14 - (6.39 \pm 2.00) \text{ S}^{3+}/\text{S}^{++}.$$

This indicates a marginal, statistically significant ( $3.2 \sigma$ ) negative slope as  $\text{S}^{3+}/\text{S}^{++}$  increases. As with Fig. 11, if we exclude the four lowest ionization galaxies and fit just the five with the highest ionization, then,

$$\text{Ne/S} = 14.42 \pm 1.30 - (2.84 \pm 1.72) \text{ S}^{3+}/\text{S}^{++}.$$

This flatter negative slope ( $1.6 \sigma$ ) is no longer statistically significant. The linear least-squares fit to the reanalyzed L08 data in Table 6 for the same 23 positions as done in Fig. 11 results in,

$$\text{Ne/S} = 12.14 \pm 0.44 - (5.69 \pm 1.88) \text{ S}^{3+}/\text{S}^{++},$$

with a slope that is borderline significant ( $3.0 \sigma$ ).

It is tantalizing to conjecture that for high ionization objects, all the dominant states of Ne and S are measured, resulting in a robust estimate of the true Ne/S abundance ratio. For objects as diverse as the Orion Nebula and NGC 3603, the M33 H II regions, 30 Dor, N 66, and the blue compact dwarf galaxies, there is remarkably little variation in the Ne/S derived. We note that if we were to adopt the smaller [S III] effective collision strengths (Galavís et al. 1995) that W08 and L08 used, all values for Ne/S that we have derived would be lower, including that for Orion. A rough estimate of how much lower is  $\sim 2$  (that is,  $\sim 15\text{--}25$  percent), which can be surmised from the comparison with the W08 and L08 Ne/S values and the recalculated values here in Tables 5 and 6. All of these Ne/S values point to a much larger ratio than the “canonical” solar value of  $\sim 5$  (see next section) and what had previously been predicted by the GCE models mentioned in the Introduction. The question, of how universal the Ne/S ratio may be, will require further study. Two of the blue compact dwarf galaxies (UM461 and IIZw40) with the highest degree of ionization strongly affect the line fits in Figures 11 and 12 and the conclusion that Ne/S continues to decrease, reaching a value of 10. It is possible that it does take such a high degree of ionization to percolate off any substantial amount of S that may still be tied up in grains, molecules, and  $\text{S}^+$ . Further *Spitzer* observations of high-ionization H II regions will be useful for this purpose. We note that the type of analysis done here will not hold for even higher ionization objects where substantial amounts of Ne exist as  $\text{Ne}^{3+}$  or higher and/or S as  $\text{S}^{4+}$  or higher.

## 8. Summary and conclusions

We have observed emission lines of H(7–6) 12.37, [Ne II] 12.81, [Ne III] 15.56, [S III] 18.71, and [S IV] 10.51  $\mu\text{m}$  cospatially with the *Spitzer Space Telescope* using the Infrared Spectrograph (IRS) in short-high mode (SH). From the measured fluxes, we estimate the ionic abundance ratios  $\text{Ne}^{++}/\text{Ne}^+$ ,  $\text{S}^{3+}/\text{S}^{++}$ , and  $\text{S}^{++}/\text{Ne}^+$  in 25 H II regions in the substantially face-on spiral galaxy M33. These nebulae cover a range from 0.71 to 6.73 kpc in deprojected galactocentric distance  $R_G$ . We find a correlation of increasingly higher ionization with increasing  $R_G$ . This is seen in the variation of  $\text{Ne}^{++}/\text{Ne}^+$ ,  $\text{S}^{3+}/\text{S}^{++}$ , and  $\langle \text{S}^{++} \rangle / \langle \text{Ne}^+ \rangle$

with  $R_G$  (see Figures 3–5). A possible reason may be due to the lower metallicity at larger  $R_G$  causing the exciting stars to have a harder ionizing spectrum. As mentioned in the introduction and discussed in considerable detail (e.g., Morisset et al. 2004), there are other effects that could mimic this. We find a decrease in the metallicity, as measured by the Ne/H and S/H ratio, with increasing  $R_G$  (see Figures 7–8). The linear-log gradients that we derive are in remarkable agreement with the recent value for the log (O/H) gradient of  $-0.054 \pm 0.011$  dex kpc $^{-1}$  (Magrini et al. 2007) derived from optical observations of 14 H II regions in M33. Because their slope is practically identical to ours for log (Ne/H), we infer a Ne/O ratio of 0.28.

By sampling the dominant ionization states of Ne and S for H II regions, we can approximate the Ne/S ratio by  $(\text{Ne}^+ + \text{Ne}^{++}) / (\text{S}^{++} + \text{S}^{3+})$ . For M33, we find no significant variation in the Ne/S ratio with  $R_G$ . Both Ne and S are the products of  $\alpha$ -chain reactions following carbon and oxygen burning in stars, with large production factors from core-collapse supernovae. Both are primary elements, making their yields depend very little on the stellar metallicity. Thus, at least to “first order”, it is expected that Ne/S remains relatively constant throughout a galaxy. As discussed in §4 and §7, our estimate for Ne/S has accounted for neither the presence of S $^+$  nor S that may be tied up in grains or molecular gas.

The data presented here for M33, combined with other *Spitzer* data (see Figures 11 and 12), are consistent with our view that there are now reliable estimates for the *total* Ne/S ratio. As long as the degree of ionization is sufficiently high such that the amount of sulfur in forms other than S $^{++}$  and S $^{3+}$  is small, the methodology used here will provide a robust total Ne/S estimate. The median Ne/S value we derive for the M33 objects is 16.3, but this includes many with relatively low ionization. Although there is no statistically significant gradient with Ne $^{++}/\text{Ne}^+$ , two of the sources, BCLMP 638 and 280, with the highest ionization are among those with the lowest Ne/S at 13.9 and 13.3, respectively. For the W08 blue compact dwarf galaxies, we find a median Ne/S for the 9 galaxies of 14.0. When we consider just the 5 with the highest ionization, the median drops to 13.2. From Table 6 with the recomputed Ne/S from the L08 observations, we find a median Ne/S of 10.1 for N 66 and 11.4 for 30 Dor. This median for 30 Dor drops to 11.3 if the three lowest ionization values are not included. Although the data are limited, we note the possibility that the true Ne/S ratio may be less for lower metallicity galaxies. N 66 has the lowest metallicity ( $\sim 0.2$  solar) while 30 Dor in the LMC has an intermediate value compared with the Milky Way. On the other hand, W08 found no correlation of Ne/S with metallicity for the blue compact dwarf galaxies.

The solar abundance, particularly of Ne, remains the subject of much controversy (e.g., Drake & Testa 2005; Bahcall, Serenelli, & Basu 2006; and references in each of these). While we cannot directly address the solar abundance with our observations of extragalactic

H II regions, it is important to have reliable benchmarks for the Ne abundance. There appears to be a growing body of evidence that the Ne abundance [its fractional number abundance relative to H log H = 12, by definition and termed  $A(H)$ ] is substantially higher in the solar neighborhood, and even in the Sun itself, than the “canonical” solar values given in two often-referenced papers. These papers have for the Sun:  $A(\text{Ne}) = 7.87$ ,  $A(\text{S}) = 7.19$  (Lodders 2003) and  $A(\text{Ne}) = 7.84$ ,  $A(\text{S}) = 7.14$  (Asplund, Grevesse, & Sauval 2005). Thus according to both,  $\text{Ne/S} \sim 5$ . It is now generally accepted that Ne has the least well determined solar abundance among the most abundant elements. One of the proponents for a higher neon abundance pointed out that an  $A(\text{Ne}) = 8.29$  would reconcile solar models with the helioseismological measurements (Bahcall, Basu, & Serenelli 2005). Using this value together with the  $A(\text{S})$  values above, we obtain  $\text{Ne/S}$  of 12.6 and 14.1, respectively, close to the Orion Nebula ratio 14.3 (Simpson et al. 2004) and the various median ratios that range from 10.1 to 16.3 derived earlier.

As discussed in the last section, there is a surprisingly large difference between the effective collision strengths calculated for [S III]. It would be very worthwhile to resolve the differences with a new calculation or possibly experimental work. This is a very important matter because the dominant sulfur ionization state in the preponderance of H II regions is  $\text{S}^{++}$ . Another desirable avenue for future work would be ground-based optical observations that could cover the  $\text{S}^+$  ion, which must be present at some level, and which cannot be done with *Spitzer*. A programme designed to cover [S II] 6716,31 Å as well as the [S III] 9069,9531 Å lines, particularly for the regions we deem high ionization here, would confirm whether or not the  $\text{S}^+$  abundance is negligible and the reliability of our  $\text{Ne/S}$  values.

In our earlier M83 paper (R07), we discussed what the  $\text{Ne/S}$  ratio was predicted to be according to calculations based on the theoretical nucleosynthesis, galactic chemical evolution models of Timmes, Woosley, & Weaver (1995). The ratio was about 3.8. Since then there have been improved models (Woosley & Heger 2007). Their calculation considers massive stars from 12 to 120  $M_\odot$  starting with the solar abundance set of Lodders (2003). One difference from the Timmes et al. work is the addition now of a treatment for mass loss. This includes mass loss on the main sequence as well as red giant, and Wolf-Rayet phases. It also includes improvements in the explosion physics and nuclear cross sections. Stellar rotation is not included and according to Stan Woosley (private communication), will have an uncertain effect. Based on Fig. 7 in Woosley & Heger (2007), the  $\text{Ne/S}$  ratio is predicted to be  $\sim 8.6$ . These models are based on starting with the solar abundances. Since several of the objects observed by *Spitzer* are lower than solar metallicity, it would be very interesting to compute the  $\text{Ne/S}$  nucleosynthesis yields starting with lower metallicities.

The data set here, combined with our previous M83 results (R07), may be used as

constraints on the ionizing SEDs for the stars exciting these nebulae by comparing the ratio of fractional ionizations  $\langle \text{Ne}^{++} \rangle / \langle \text{S}^{++} \rangle$ ,  $\langle \text{Ne}^{++} \rangle / \langle \text{S}^{3+} \rangle$ , and  $\langle \text{Ne}^{++} \rangle / \langle \text{Ne}^+ \rangle$  vs.  $\langle \text{S}^{3+} \rangle / \langle \text{S}^{++} \rangle$  with predictions made from our photoionization models using stellar atmosphere models from several different sources. In Figures 9a,b we show the comparison assuming that the Ne/S ratio does not vary and equals the Orion Nebula value. Generally, the best fit is to the nebular models using the supergiant stellar atmosphere models (Pauldrach et al. 2001) computed with the WM-BASIC code. The comparison shown in Figure 9c is independent of the Ne/S ratio. For the most part, the  $\text{Ne}^{++}/\text{Ne}^+$  values appear to lie closer to the theoretical loci that use the Martins et al., Lanz & Hubeny et al., and Pauldrach et al. *dwarf* SEDs. While the  $\text{Ne}^{++}/\text{Ne}^+$  ratio has the advantage of being independent of elemental abundance ratios, it appears to be more sensitive to the *nebular* parameters than does the other ionic ratios used in Figures 9 and 10. This fact tends to make it less unique in its ability to discriminate between the stellar SEDs we present in this paper. We note that these comparisons are mainly qualitative since these ionic ratios depend not only on the SED, but also on the nebular parameters discussed as well as the effects of the stellar metallicity on the SED.

This work is based on observations made with the *Spitzer Space Telescope*, which is operated by the Jet Propulsion Laboratory, California Institute of Technology under NASA contract 1407. Support for this work was provided by NASA for this *Spitzer* programme identification 20057. We thank Stan Woosley for providing information on the Ne/S ratio from a nucleosynthesis, galactic chemical evolution perspective. The referee Christophe Morisset provided comments that helped improve the paper. Our computer support at NASA Ames was handled very well by David Goorvitch. We thank Danny Key, Erik Krasner-Karpen, and Matt Lattanzi for assistance with the data reduction. The nebular models were run on JPL computers, initially a Cray and more recently, a Dell Intel Xeon cluster. Funding for computer use in this investigation was provided by the JPL Office of the Chief Information Officer. We are grateful to Heidi Lorenz-Wirzba for excellent computer support.

## REFERENCES

Afflerbach A., Churchwell E., Werner M.W., 1997, ApJ, 478, 190

Asplund M., Grevesse N., Sauval A.J., 2005, in Cosmic Abundances as Records of Stellar Evolution and Nucleosynthesis, ed. T.G. Barnes III, F.N. Bash, ASP Conf. Ser., 336, 25

Bahcall J.N., Basu S., Serenelli A.M., 2005, ApJ, 631, 1281

Bahcall J.N., Serenelli A.M., Basu S., 2006, ApJS, 165, 400

Boulesteix J., Courtès G., Laval A., Monnet G., Petit H., 1974, A&A, 37, 33

Bresolin F., Kennicutt R.C. Jr., 2002, ApJ, 572, 838

Butler K., Zeippen C.J., 1994, A&A, 108, 1

Chiappini C., Matteucci F., Romano D., 2001, ApJ, 554, 1044

Chiappini C., Romano D., Matteucci F., 2003, MNRAS, 339, 63

Churchwell E., Smith L.F., Mathis J., Mezger P.G., Huchtmeier W., 1978, A&A, 70, 719

Corbelli E., Schneider S.E., 1997, ApJ, 479, 244

Cotton W.D., Condon J.J., Arbizzani E., 1999, ApJS, 125, 409

Crockett N.R., Garnett D.R., Massey P., Jacoby G., 2006, ApJ, 637, 741

Drake J.J., Testa P., 2005, Nature, 436, 525

Dufour R.J., Talbot R.J. Jr., Jensen E.B., Shields G.A., 1980, ApJ, 236, 119

Freedman W.L., Wilson C.D., Madore B.F., 1991, ApJ, 372, 455

Galavís M.E., Mendoza C., Zeippen C.J., 1995, A&AS, 111, 347

Giveon U., Sternberg A., Lutz D., Feuchtgruber H., Pauldrach A.W.A., 2002, ApJ, 566, 880

Henry R.B.C., Worthey G., 1999, PASP, 111, 919

Higdon S.J.U., et al., 2004, PASP, 116, 975

Hou J.L., Prantzos N., Boissier S., 2000, A&A, 362, 921

Houck J.R., et al., 2004, ApJS, 154, 18

Kurucz R.L., 1992, in IAU Symp. 149, Stellar Population of Galaxies, ed. B. Barbuy A. Renzini, p. 225

Lanz T., Hubeny I., 2003, ApJS, 146, 417

Lebouteiller V., Bernard-Salas J., Brandl B., Whelan D.G., Wu Y., Charmandaris V., Devost D., Houck J.R., 2008, ApJ (in press) astro-ph/0710.4549 (L08)

Lodders K., 2003, ApJ, 591, 1220

Magrini L., Vílchez J.M., Mampaso A., Corradi R.L.M., Leisy P., 2007, A&A, 470, 865

Martín-Hernández N.L., et al., 2002a, A&A, 381, 606

Martín-Hernández N.L., Vermeij R., Tielens A.G.G.M., van der Hulst J.M., Peeters E., 2002b, A&A, 389, 286

Martins F., Schaerer D., Hillier D.J., 2005, A&A, 436, 1049

McLaughlin B.M., Bell K.L., 2000, JPhysB, 33, 597

Mokiem M.R., Martín-Hernández N.L., Lenorzer A., de Koter A., Tielens A.G.G.M., 2004, A&A, 419, 319

Morisset C., Schaerer D., Bouret J.-C., Martins F., 2004, A&A, 415, 577

Pagel B.E.J., 2001, PASP, 113, 137

Pagel B.E.J., Edmunds, M.G., 1981, ARA&A, 19, 77

Pauldrach A.W.A., Hoffmann T.L., Lennon M., 2001, A&A, 375, 161

Peimbert M., 1967, ApJ, 150, 825

Rodríguez M., Rubin R.H., 2005, ApJ, 626, 900

Rolleston W.R.J., Smartt S.J., Dufton P.L., Ryans R.S.I., 2000, A&A, 363, 537

Rubin R.H., 1968, ApJ, 154, 391

Rubin R.H., et al., 2006, in Combes F., Palous J., eds, Proc. IAU Symp. 235, Galaxy Evolution Across the Hubble Time. Cambridge Univ. Press, Cambridge, p. 326

Rubin R.H., Simpson J.P., Colgan S.W.J., Dufour R.J., Ray K.L., Erickson E.F., Haas M.R., Pauldrach A.W.A., Citron R.I., 2007, MNRAS, 377, 1407 (R07)

Rubin R.H., Simpson J.P., Lord S.D., Colgan S.W.J., Erickson E.F., Haas M.R., 1994, ApJ, 420, 772

Rudolph A.L., Fich M., Bell G.R., Norsen T., Simpson J.P., Haas M.R., Erickson E.F., 2006, ApJS, 162, 346

Sandford S.A., Pendleton Y.J., & Allamandola L.J., 1995, ApJ, 440, 697

Saraph H.E., Storey P.J., 1999, A&AS, 134, 369

Saraph H.E., Tully J.A., 1994, A&AS, 107, 29

Seaton M.J., 1959, MNRAS, 119, 81

Shaver P.A., McGee R.X., Newton L.M., Danks A.C., Pottasch S.R., 1983, MNRAS, 204, 53

Shields G.A., 2002, RMxAC, 12, 189

Simpson J.P., Colgan S.W.J., Cotera A.S., Erickson E.F., Hollenbach D.J., Kaufman M.J., Rubin R.H., 2007, ApJ, 670, 1115

Simpson J.P., Colgan S.W.J., Rubin R.H., Erickson E.F., Haas M.R., 1995, ApJ, 444, 721

Simpson J.P., Rubin R.H., 1990, ApJ, 354, 165

Simpson J.P., Rubin R.H., Colgan S.W.J., Erickson E.F., Haas M.R., 2004, ApJ, 611, 338

Smith L.J., Norris R.P.F., Crowther P.A., 2002, MNRAS, 337, 1309

Smith J.D.T., et al., 2007a, PASP, 119, 1133

Smith J.D.T., et al., 2007b, CUBISM Handbook

Sternberg A., Hoffmann T.L., Pauldrach A.W.A., 2003, ApJ, 599, 1333

Storey P.J., Hummer D.G., 1995, MNRAS, 272, 41

Tayal S.S., Gupta G.P., 1999, ApJ, 526, 544

Thum C., Mezger P.G., Pankonin V., 1980, A&A, 87, 269

Timmes F.X., Woosley S.E., Weaver T.A., 1995, ApJS, 98, 617

Vílchez J.M., Pagel B.E.J., Díaz A.I., Terlevich E., Edmunds M.G., 1988, MNRAS, 235, 633

Willner S.P., Nelson-Patel, K., 2002, ApJ, 568, 679

Woosley S.E., Heger A., 2007, PhR, 442, 269

Wu Y., Bernard-Salas J., Charmandaris V., Lebouteiller V., Hao L., Brandl B.R., Houck J.R., 2008, ApJ, 673, 193 (W08)

Zaritsky D., Elston R., Hill J.M., 1989, AJ, 97, 97

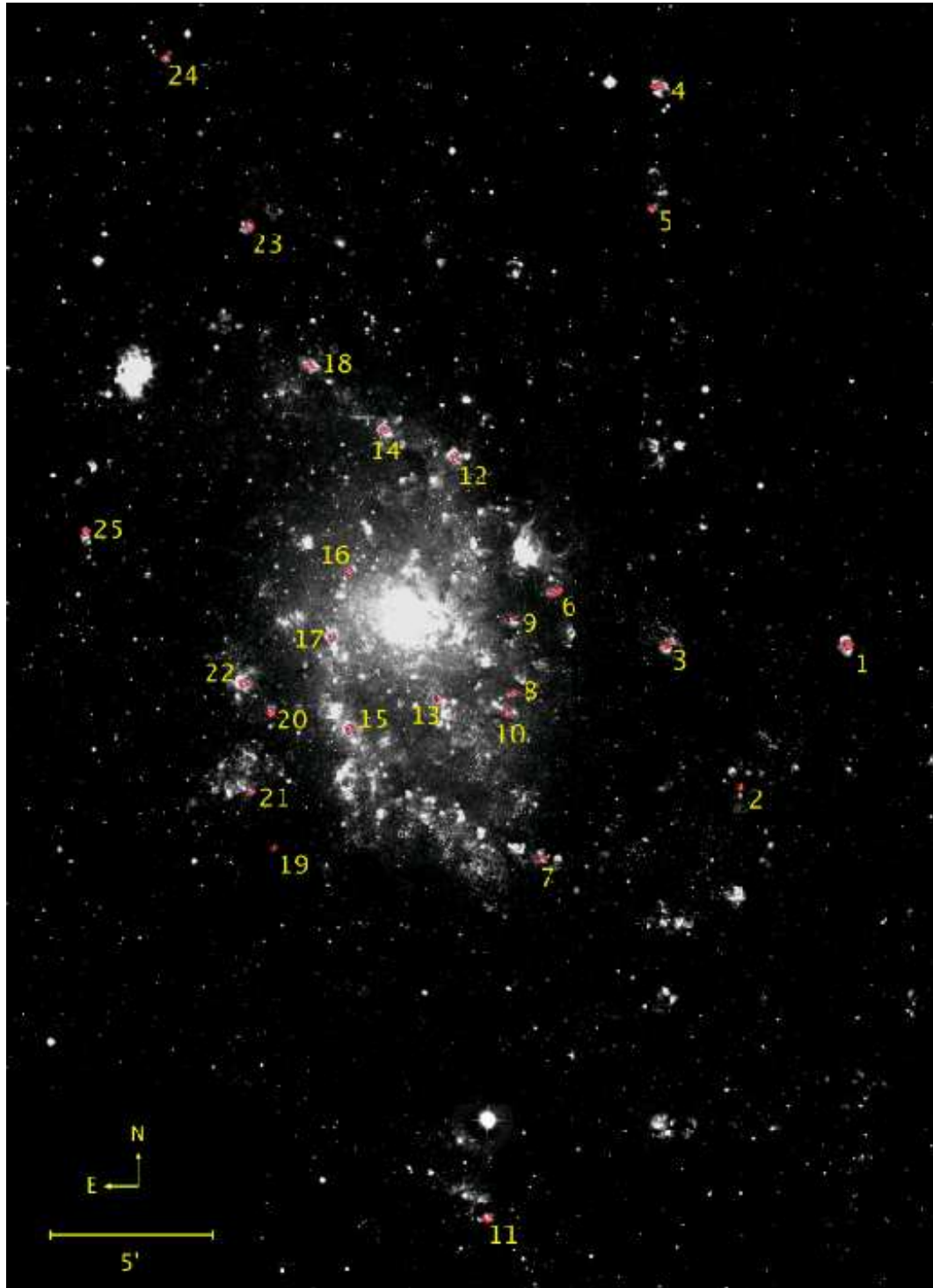


Fig. 1.— The positions and apertures observed for 25 H II regions are shown superimposed on an H $\alpha$  image of the substantially face-on (tilt 56°) M33. The nebulae are numbered W to E (see Table 1). N is up and E left.

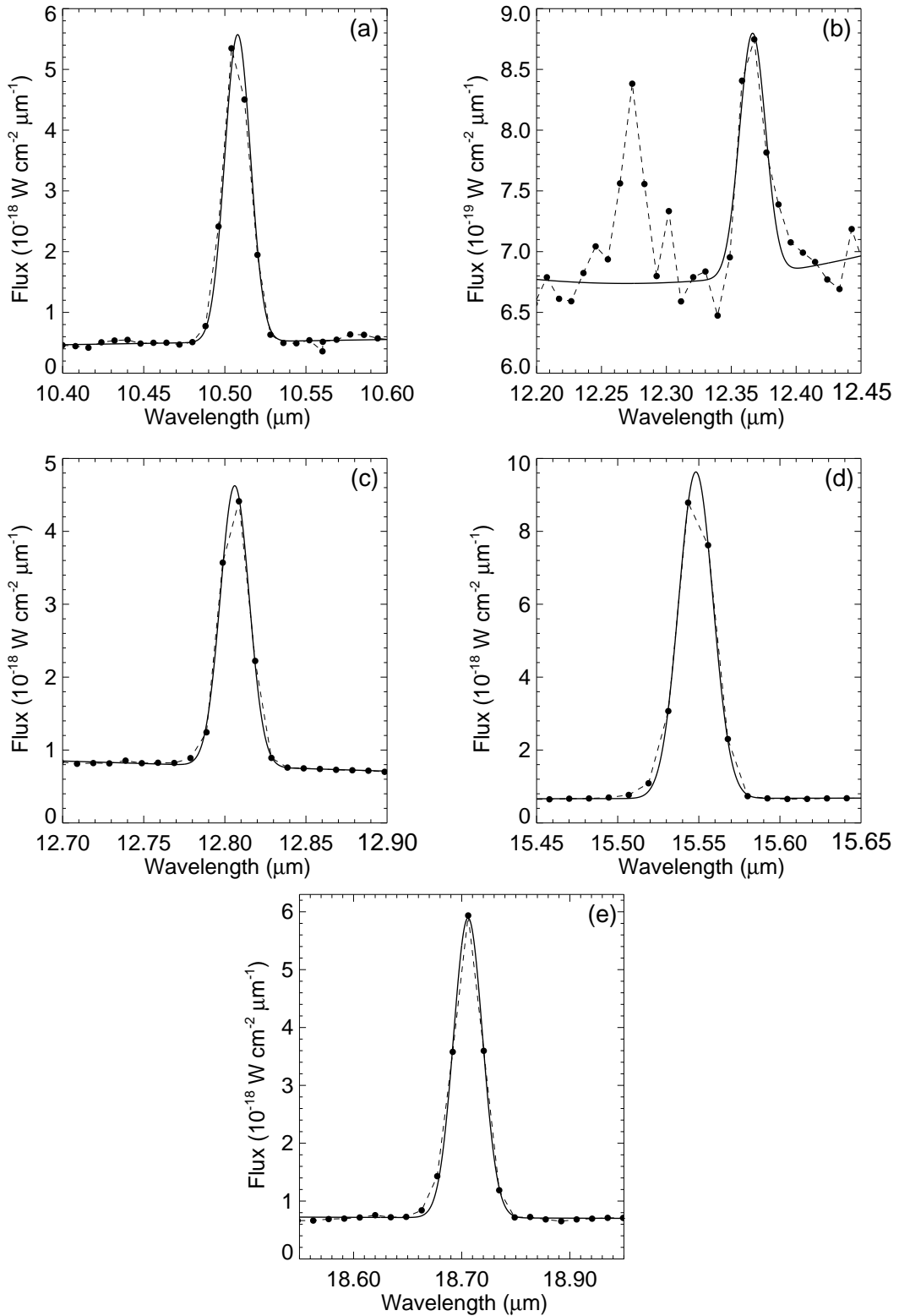


Fig. 2.— Measurements of the five emission lines in the H II region BCLMP 45 (#6 in Fig. 1): (a) [S IV] 10.5  $\mu\text{m}$ ; (b) H(7-6) 12.4  $\mu\text{m}$ ; the feature on the blue side is  $\text{H}_2$  S(2); (c) [Ne II] 12.8  $\mu\text{m}$ ; (d) [Ne III] 15.6  $\mu\text{m}$ ; and (e) [S III] 18.7  $\mu\text{m}$ . The data points are the filled circles. The fits to the continuum and Gaussian profiles are the solid lines. Such measurements provide the set of line fluxes for further analysis.

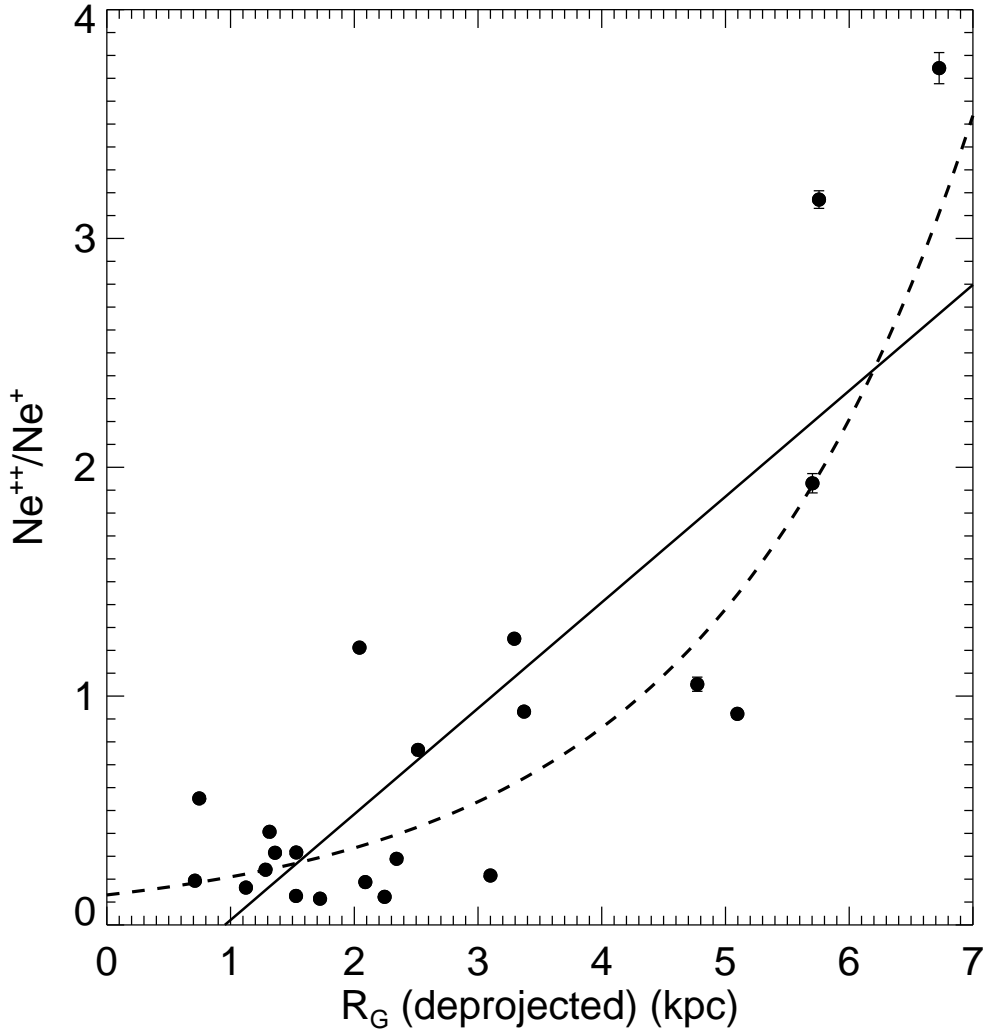


Fig. 3.— Plot of the ionic abundance ratio  $N_{e^{++}}/N_{e^+}$ , which is derived from the measured line flux ratios for 22 of the H II regions, vs.  $R_G$ . We assume an electron density ( $N_e$ ) of  $100 \text{ cm}^{-3}$ . There is extremely little change with  $N_e$  over the range expected for these regions. The solid line is a linear least-squares fit while the dashed line results from a linear least-squares fit to these points in a  $\log(N_{e^{++}}/N_{e^+})$  vs.  $R_G$  plot. In both cases, there is a significant positive correlation with  $R_G$ . Error bars here and in Figs 4–8 are for the propagated measurement uncertainties and do not include the systematic uncertainties (see text).

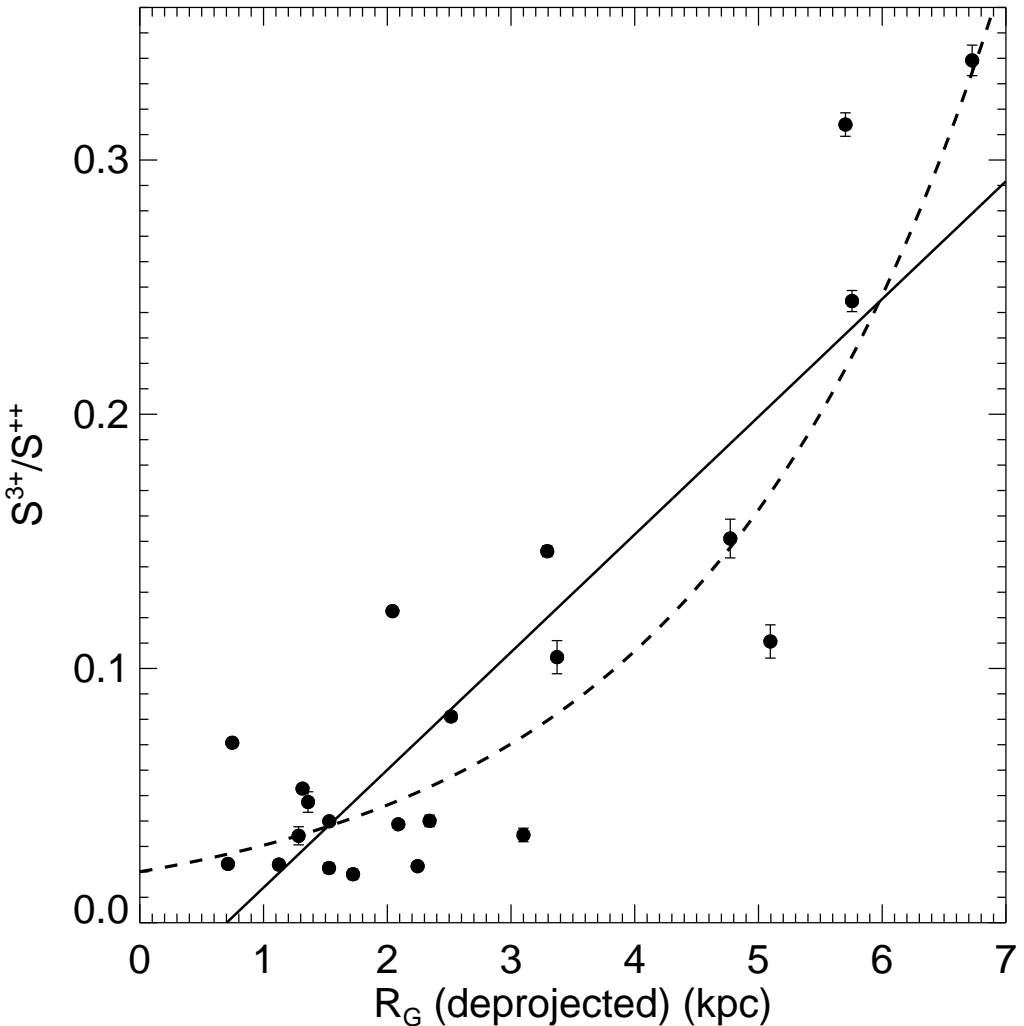


Fig. 4.— Plot of the ionic abundance ratio  $S^{3+}/S^{++}$  vs.  $R_G$  for the same 22 H II regions as Figure 3. Here also, we assume  $N_e$  of  $100 \text{ cm}^{-3}$ . The solid line is a linear least-squares fit while the dashed line results from a linear least-squares fit to these points in a  $\log(S^{3+}/S^{++})$  vs.  $R_G$  plot. In both cases, there is a significant positive correlation with  $R_G$  (see text).

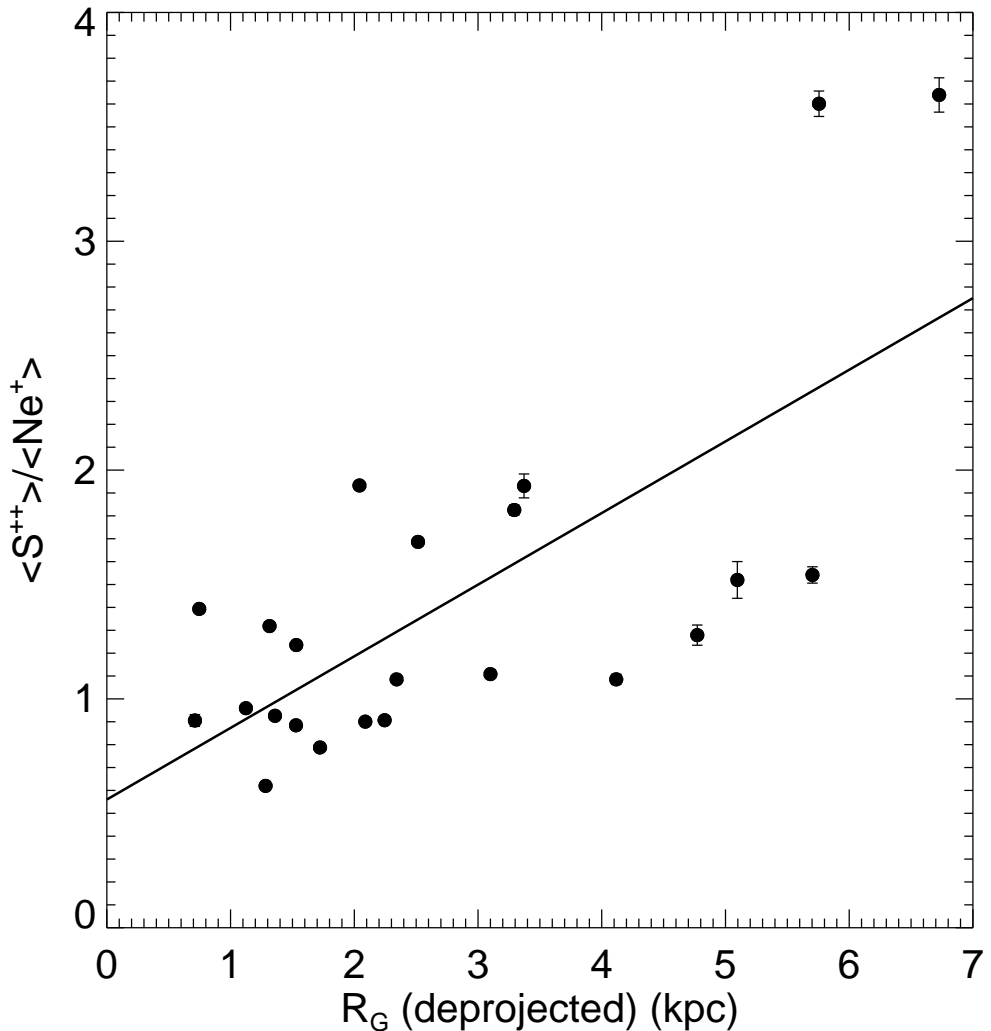


Fig. 5.— The fractional ionic abundance ratio  $\langle S^{++} \rangle / \langle Ne^+ \rangle$  vs.  $R_G$  for 23 H II regions. The linear least-squares fit for an assumed  $N_e$  of  $100 \text{ cm}^{-3}$  is shown. The plotted  $\langle S^{++} \rangle / \langle Ne^+ \rangle$  ratio assumes an Orion Nebula Ne/S abundance ratio of 14.3 (Simpson et al. 2004).

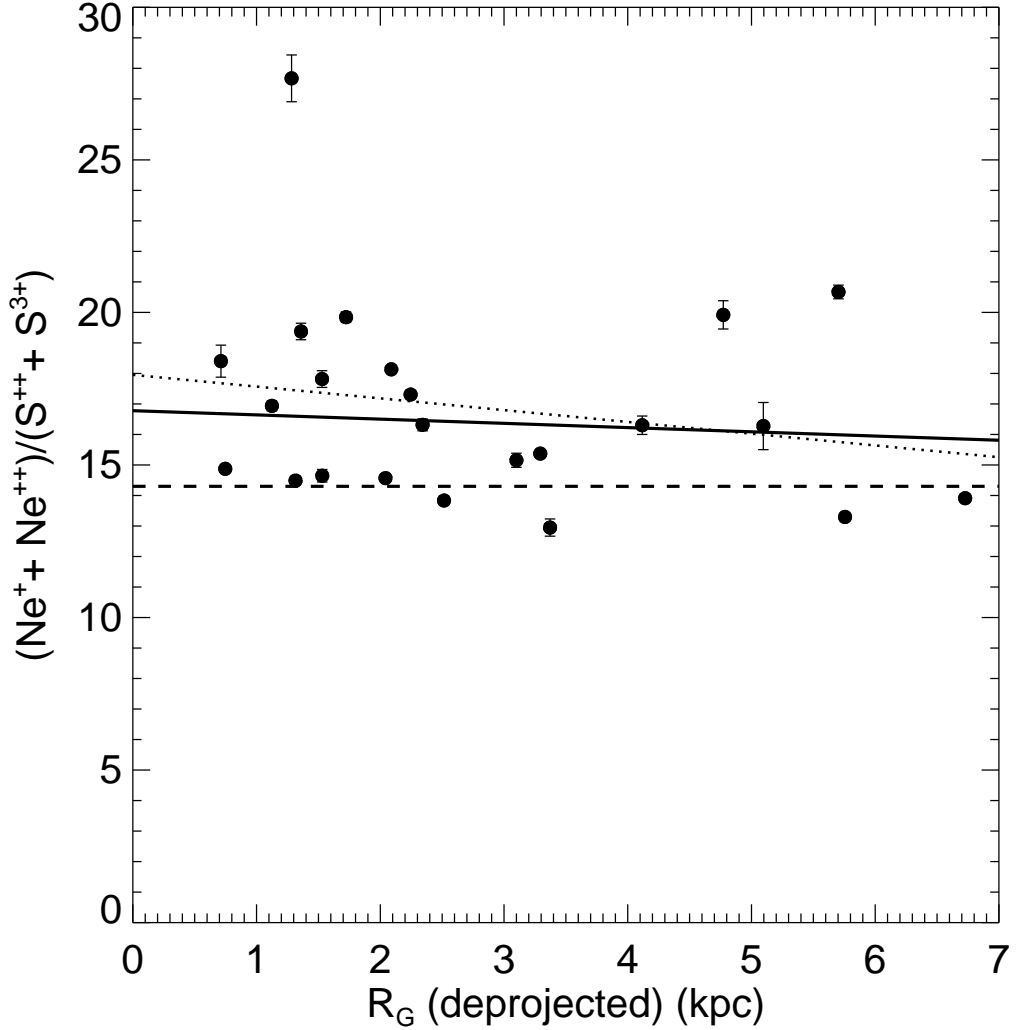


Fig. 6.— Ne/S, as approximated by  $(\text{Ne}^+ + \text{Ne}^{++})/(\text{S}^{++} + \text{S}^{3+})$  vs.  $R_G$ . We fit the points with a linear least-squares function two ways: using 23 points (omitting source 230 and 702) (dotted line) and 22 points, excluding in addition the most deviant value shown, source 32 (solid line). For both fits, there is no significant variation in the Ne/S ratio with  $R_G$ . For reference, the dashed line depicts a constant Ne/S = 14.3, the Orion Nebula value.

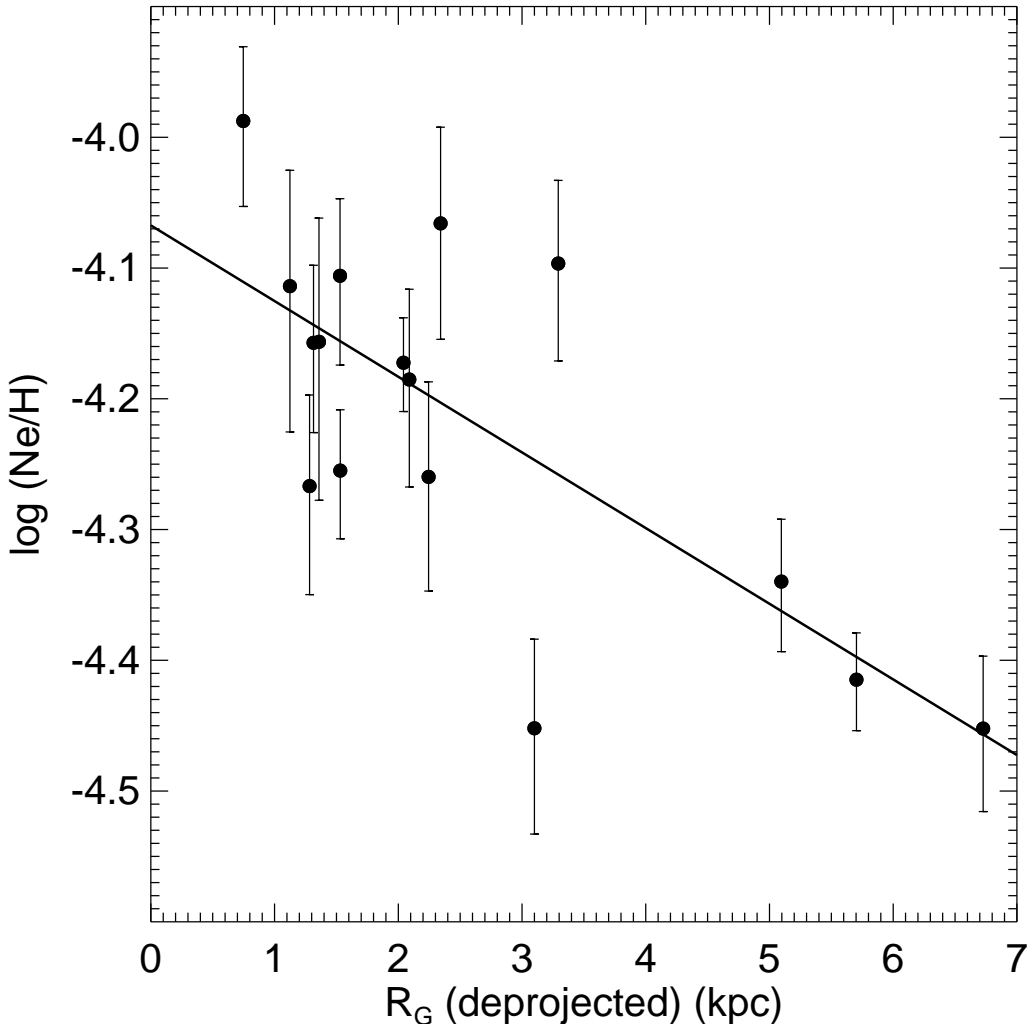


Fig. 7.— Plot of  $\log (\text{Ne}/\text{H})$  vs.  $R_G$  for 16 sources in M33. The linear least-squares fit is  $\log (\text{Ne}/\text{H}) = -4.07 \pm 0.04 - (0.058 \pm 0.014) R_G$ . This Ne/H plot is our most reliable indicator of metallicity and of a determination of a significant metallicity gradient with increasing  $R_G$ .

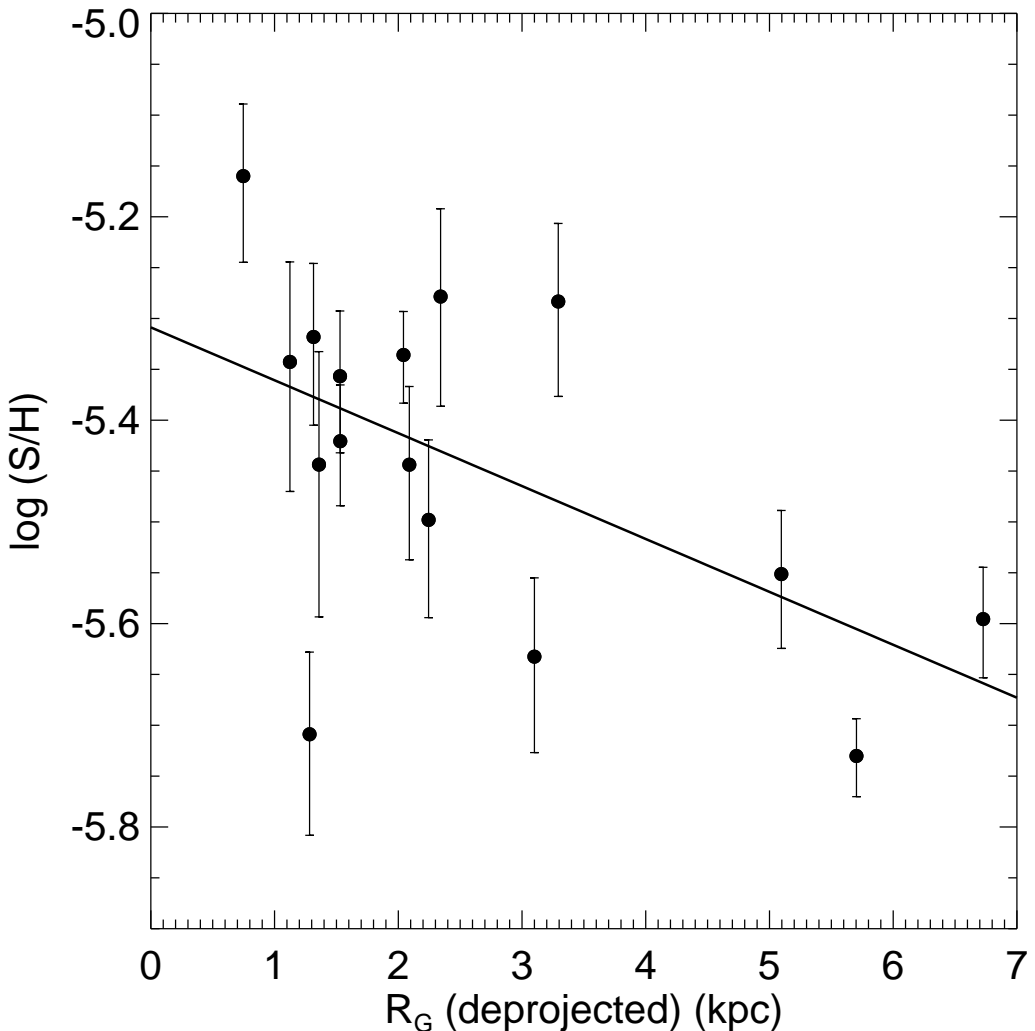


Fig. 8.— Plot of  $\log (\text{S}/\text{H})$  vs.  $R_G$  for 16 sources in M33. The linear least-squares fit is  $\log (\text{S}/\text{H}) = -5.31 \pm 0.06 - (0.052 \pm 0.021) R_G$ . The gradient is similar to that from the Ne/H fit but statistically less significant ( $2.5 \sigma$ ). As discussed in text, this sulfur value does not account for S<sup>+</sup> or for S that may be in dust or molecules.

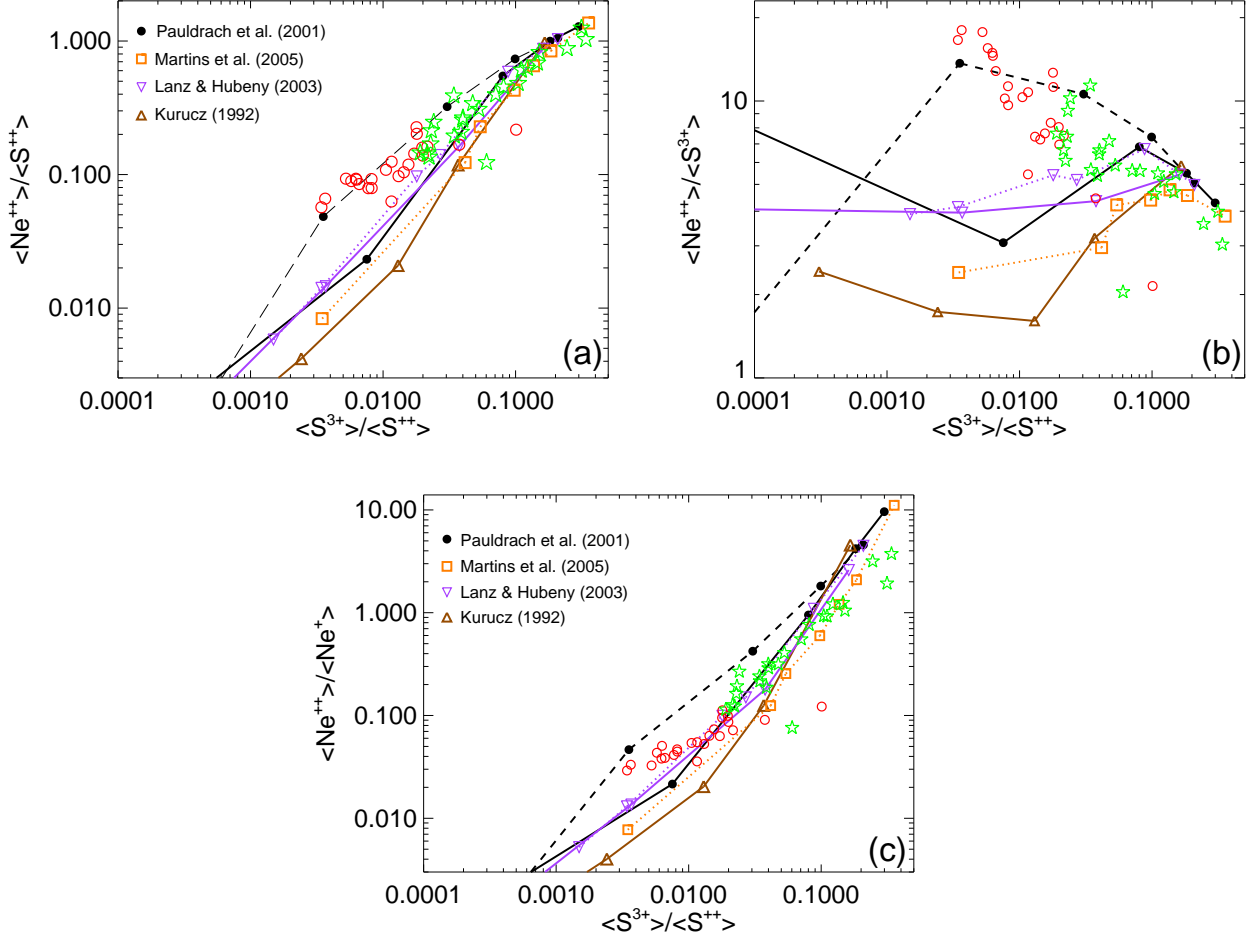


Fig. 9.— **(a)** Theoretical predictions of the fractional ionization ratios  $\langle \text{Ne}^{++} \rangle / \langle \text{S}^{++} \rangle$  vs.  $\langle \text{S}^{3+} \rangle / \langle \text{S}^{++} \rangle$ , computed using our photoionization code NEBULA. The lines connect the results of nebular models calculated with the ionizing SEDs predicted from various stellar atmosphere models as labeled, changing no other parameter except the SED. For the H II region models calculated with Pauldrach et al. atmospheres, the solid line connects models with dwarf atmospheres and the dashed line connects models with supergiant atmospheres. The violet loci join models calculated with Lanz & Hubeny atmospheres: solid line with  $\log g = 4.0$  and the dotted line a set with smaller  $\log g$ . The dotted orange line connects models using Martins et al. atmospheres. The brown line presents results using Kurucz atmospheres. The values for  $T_{\text{eff}}$  and  $\log g$  for the specific atmospheres used are described in the text. To compare our data with the models, we need to divide the observed  $\text{Ne}^{++}/\text{S}^{++}$  and  $\text{Ne}^{++}/\text{S}^{3+}$  ratios by an assumed Ne/S abundance ratio. We use the Orion Nebula  $\text{Ne}/\text{S} = 14.3$ . The open red circles are our prior results for the M83 H II regions. The green stars are the M33 results derived from our observed line fluxes using  $N_e$  of  $100 \text{ cm}^{-3}$ .

(b) The same as panel (a) except the ordinate is  $\langle \text{Ne}^{++} \rangle / \langle \text{S}^{3+} \rangle$ . Both panels dramatically illustrate the sensitivity of the H II region model predictions of these ionic abundance ratios to the ionizing SED that is input to nebular plasma simulations. These data, for the most part, appear to track the Pauldrach et al. supergiant locus.

(c) Similar to panels (a) and (b) except the ordinate is  $\langle \text{Ne}^{++} \rangle / \langle \text{Ne}^+ \rangle$ . This plot also illustrates the sensitivity of the H II region model predictions of this ionic abundance ratio to the ionizing SED that is input to nebular plasma simulations. These data, for the most part, appear to lie closer to Martins et al., Lanz & Hubeny et al., and Pauldrach et al. *dwarf* loci.

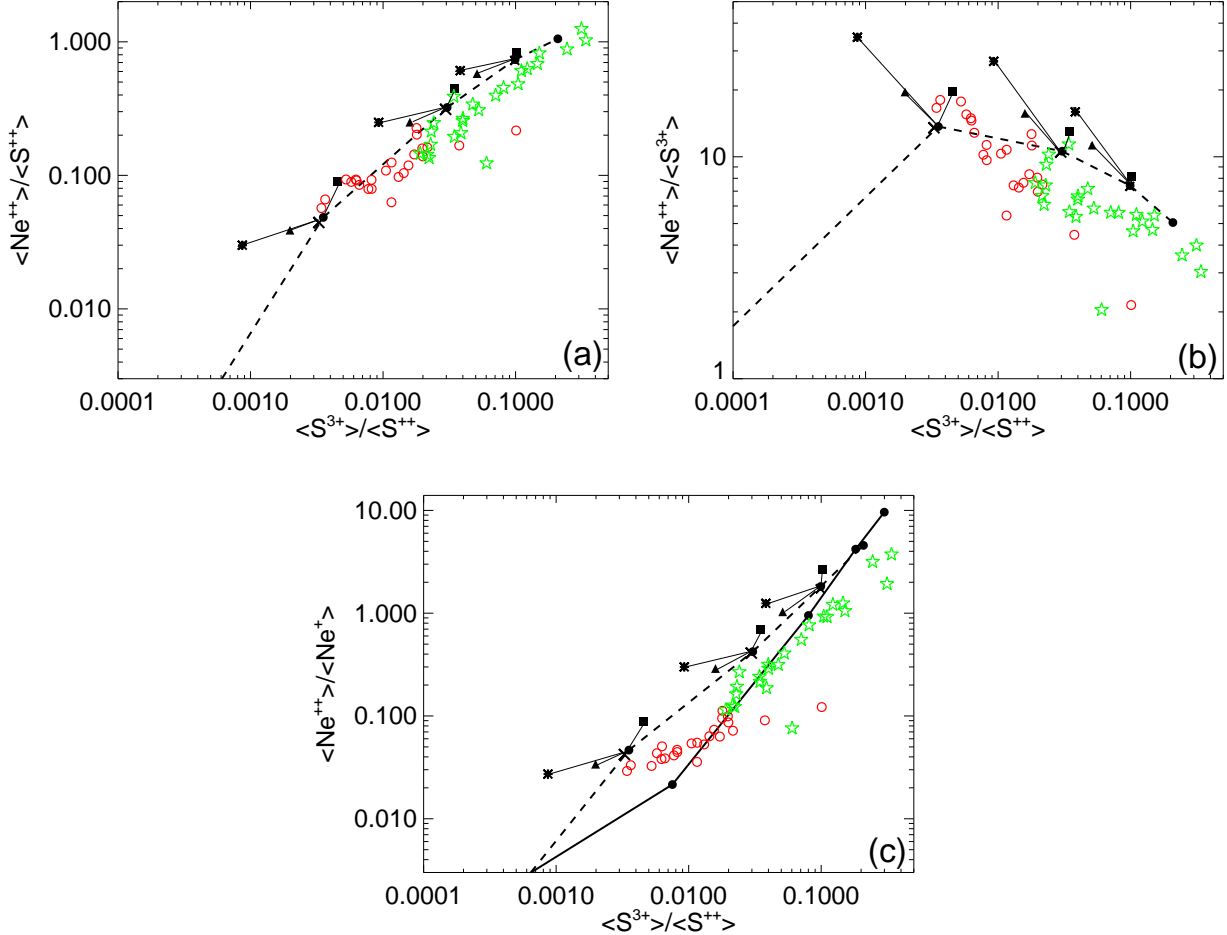


Fig. 10.— (a) This is similar to Figure 9a. We again show the locus that uses the Pauldrach et al. (2001) supergiant atmospheres. Here we display the results of making some changes to the *nebular parameters* for the  $T_{\text{eff}} = 35000, 40000$ , and  $45000$  K stellar atmospheres. The points with an \* are for a model with a central cavity of radius  $0.5$  pc (see text); those with a triangle have a density of  $100$  instead of  $1000$  cm $^{-3}$ ; those with an X have a larger number of Lyman continuum photons s $^{-1}$  ( $N_{LyC}$ ) =  $10^{50}$  instead of  $10^{49}$ ; those with a square have all heavy element abundances in the nebular set decreased by a factor of three. The thin solid lines, emanating from the standard model points, trace the change due to each of the four above modifications. Again, the open circles are from our M83 data while the open stars are the new M33 results. (b) This is similar to Figure 9b with the same modifications as described for panel (a). (c) This is similar to Figure 9c with the same modifications as described for panel (a). Here we also replot the Pauldrach et al. dwarf locus. A colour version of this figure is available in the electronic edition.

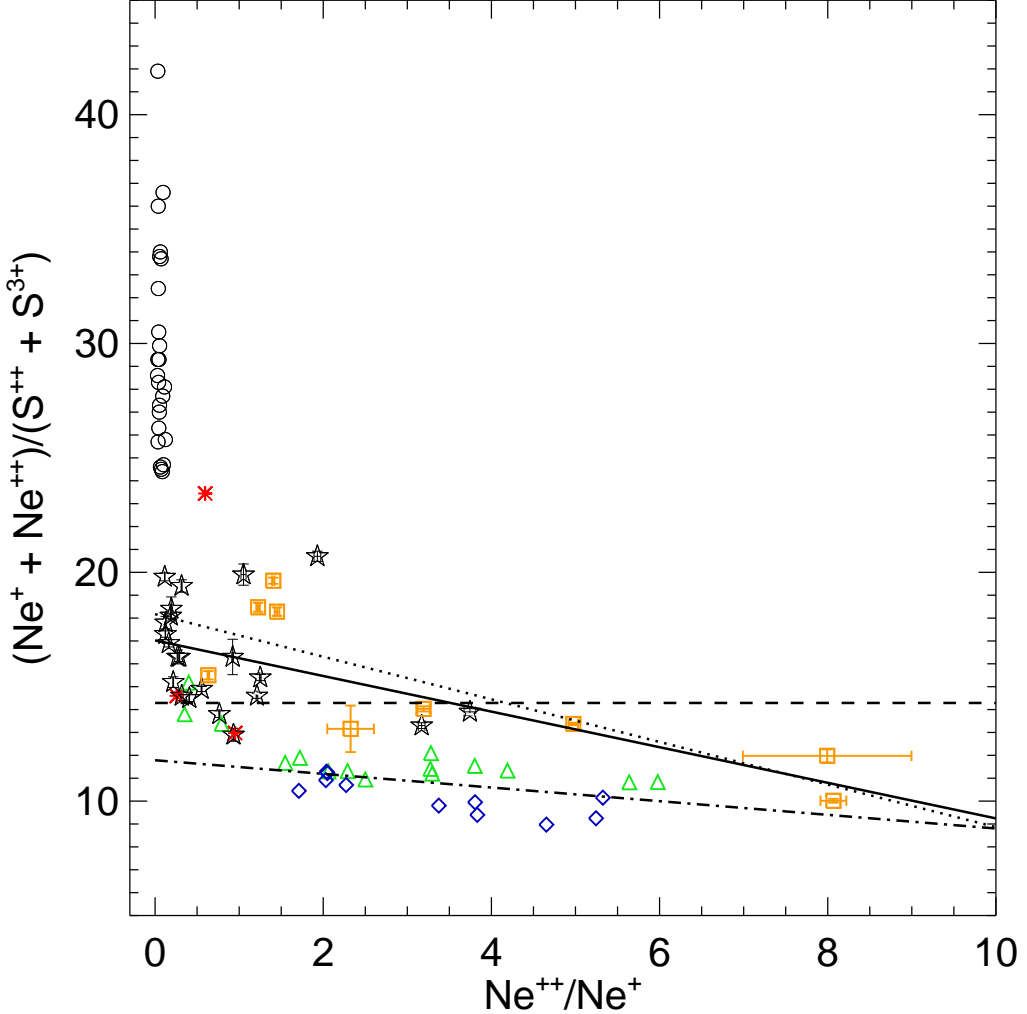


Fig. 11.— Plot of Ne/S vs.  $\text{Ne}^{++}/\text{Ne}^+$ . Here we show our M33 results as stars for the 22 sources mentioned in Fig. 6. The solid line is the linear least-squares fit to the stars with a gradient that is not statistically significant. The results from our prior M83 study are shown as circles. No line fit is done. These data demonstrate a huge variation in the inferred Ne/S ratio when  $\text{Ne}^{++}/\text{Ne}^+$  is low. The orange squares show the Wu et al. (2008) data for blue compact dwarf galaxies, as reanalyzed with our programme. We show only 9 points, those objects where they actually detected *all four* lines: [S IV], [Ne II], [Ne III], and [S III]. The rendition of their data is what we list in columns 2–4 of Table 5. The dotted line is the linear least-squares fit to the squares with a statistically significant negative slope ( $3.8 \sigma$ ). The median (average) Ne/S for the 9 galaxies is 14.0 (14.9), very close to the Orion value of 14.3 shown as the dashed line. The Lebouteiller et al. (2008) data were also reanalyzed here and are presented as follows: NGC 3603 (red asterisks), 30 Dor (green triangles), and N 66 (blue diamonds). The median Ne/S ratios for each are 14.6, 11.4, and 10.1, respectively, possibly indicating a decreasing trend with lower metallicity. The dash-dot line is a fit to the 23 points in 30 Dor and N 66 that show the highest ionization (see text).

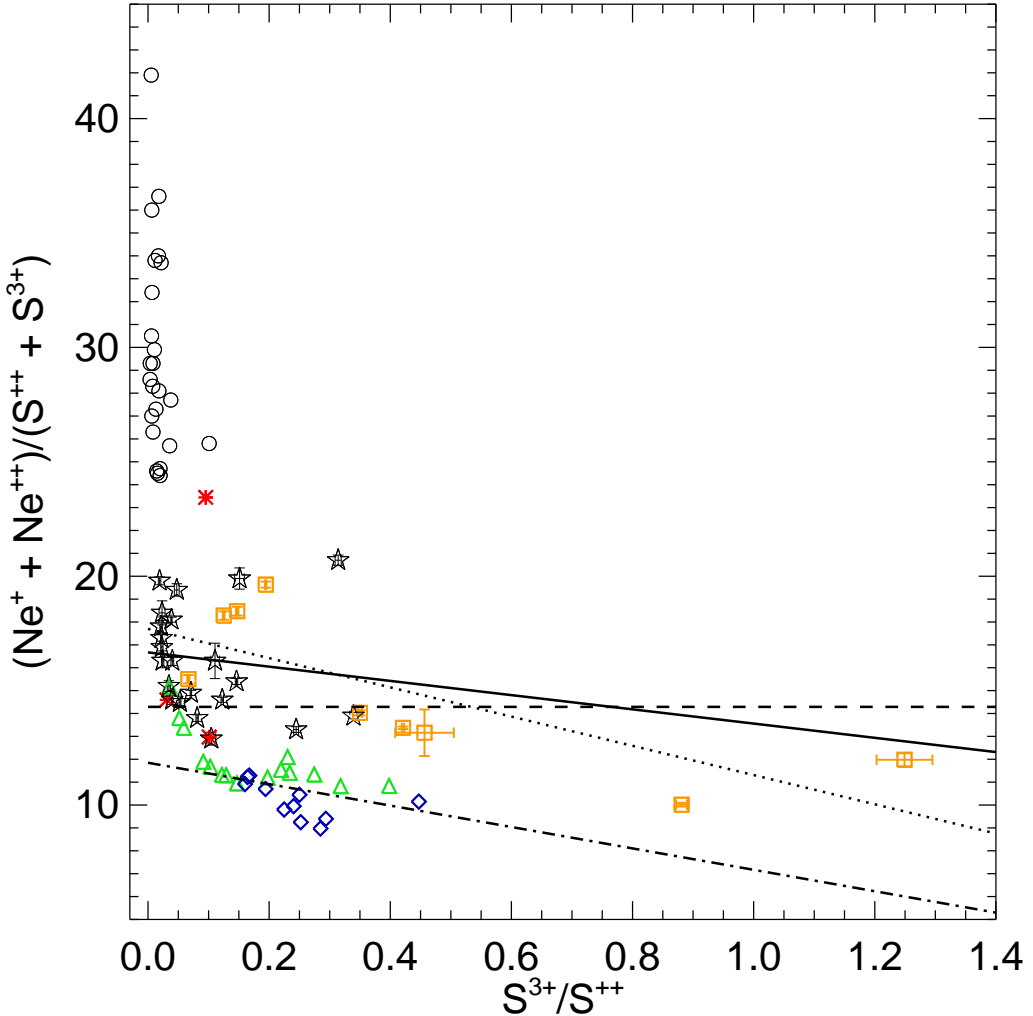


Fig. 12.— Plot of Ne/S vs.  $S^{3+}/S^{++}$  that is similar to Fig. 11. Again, the fit to the M33 points results in a gradient that is not statistically significant. The M83 points show a huge variation in the inferred Ne/S ratio at low ionization, when  $S^{3+}/S^{++}$  is small. On the other hand, our fit to the Wu et al. (2008) data produces a significant gradient ( $3.2\sigma$ ). The least-squares fit to the Lebouteiller et al. (2008) data is for the same 23 points in 30 Dor and N 66 as used in the line fit in Fig. 11.

Table 1. H II Regions Observed in M33

| Order | H II Region | RA        | J2000 | DEC      | Aperture Grid |
|-------|-------------|-----------|-------|----------|---------------|
| 1     | 280         | 1 32 45.4 |       | 30 38 56 | 2x4           |
| 2     | 230         | 1 33 00.7 |       | 30 34 17 | 1x3           |
| 3     | 277         | 1 33 12.2 |       | 30 38 49 | 2x3           |
| 4     | 638         | 1 33 16.0 |       | 30 56 45 | 2x3           |
| 5     | 623         | 1 33 16.4 |       | 30 52 47 | 1x3           |
| 6     | 45          | 1 33 29.2 |       | 30 40 25 | 2x3           |
| 7     | 214         | 1 33 30.0 |       | 30 31 47 | 1x3           |
| 8     | 33          | 1 33 34.9 |       | 30 37 06 | 1x3           |
| 9     | 42          | 1 33 35.6 |       | 30 39 30 | 1x2           |
| 10    | 32          | 1 33 35.8 |       | 30 36 29 | 1x3           |
| 11    | 251         | 1 33 36.7 |       | 30 20 13 | 1x3           |
| 12    | 62          | 1 33 44.7 |       | 30 44 38 | 1x3           |
| 13    | 27          | 1 33 46.1 |       | 30 36 54 | 1x2           |
| 14    | 301         | 1 33 55.6 |       | 30 45 27 | 1x3           |
| 15    | 4           | 1 33 59.3 |       | 30 35 48 | 1x3           |
| 16    | 79          | 1 34 00.2 |       | 30 40 51 | 1x3           |
| 17    | 87E         | 1 34 02.3 |       | 30 38 45 | 1x3           |
| 18    | 302         | 1 34 06.9 |       | 30 47 27 | 1x3           |
| 19    | 702         | 1 34 10.2 |       | 30 31 54 | 1x2           |
| 20    | 95          | 1 34 11.2 |       | 30 36 16 | 1x3           |
| 21    | 710         | 1 34 13.8 |       | 30 33 44 | 1x3           |
| 22    | 88W         | 1 34 15.3 |       | 30 37 11 | 1x3           |
| 23    | 691         | 1 34 16.5 |       | 30 51 56 | 1x3           |
| 24    | 651         | 1 34 29.8 |       | 30 57 15 | 1x3           |
| 25    | 740W        | 1 34 39.8 |       | 30 41 54 | 1x3           |

Table 2. M33 Line Measurements

| Order | Source | Line<br>μm | Flux<br>W cm <sup>-2</sup> | 1σ error<br>W cm <sup>-2</sup> | FWHM<br>km s <sup>-1</sup> | V <sub>helio</sub><br>km s <sup>-1</sup> |
|-------|--------|------------|----------------------------|--------------------------------|----------------------------|--|
| 1     | 280    | 10.5       | 5.71E-20                   | 7.76E-22                       | 530                        | -124                                     |
|       |        | 12.4       | 1.18E-21 <sup>a</sup>      | 4.28E-22                       | 734                        | -55                                      |
|       |        | 12.8       | 1.31E-20                   | 1.52E-22                       | 496                        | -195                                     |
|       |        | 15.6       | 9.50E-20                   | 3.51E-22                       | 472                        | -147                                     |
|       |        | 18.7       | 4.96E-20                   | 5.24E-22                       | 493                        | -127                                     |
| 2     | 230    | 10.5       |                            |                                |                            |  |
|       |        | 12.4       |                            |                                |                            |  |
|       |        | 12.8       | 6.00E-21                   | 1.46E-22                       | 578                        | -126                                     |
|       |        | 15.6       | 7.90E-22                   | 2.33E-22                       | 689                        | -68                                      |
|       |        | 18.7       | 2.90E-21                   | 1.90E-22                       | 505                        | -89                                      |
| 3     | 277    | 10.5       | 1.69E-20                   | 9.94E-22                       | 556                        | -147                                     |
|       |        | 12.4       |                            |                                |                            |  |
|       |        | 12.8       | 1.69E-20                   | 2.94E-22                       | 481                        | -207                                     |
|       |        | 15.6       | 3.61E-20                   | 2.32E-22                       | 469                        | -212                                     |
|       |        | 18.7       | 3.43E-20                   | 7.36E-22                       | 588                        | -230                                     |
| 4     | 638    | 10.5       | 4.94E-20                   | 6.96E-22                       | 534                        | -150                                     |
|       |        | 12.4       | 1.93E-21                   | 2.75E-22                       | 588                        | -185                                     |
|       |        | 12.8       | 8.08E-21                   | 1.42E-22                       | 621                        | -208                                     |
|       |        | 15.6       | 6.92E-20                   | 3.02E-22                       | 473                        | -191                                     |
|       |        | 18.7       | 3.09E-20                   | 3.42E-22                       | 491                        | -178                                     |
| 5     | 623    | 10.5       | 7.45E-20                   | 8.72E-22                       | 537                        | -203                                     |
|       |        | 12.4       | 4.21E-21                   | 3.26E-22                       | 588                        | -276                                     |
|       |        | 12.8       | 3.11E-20                   | 6.62E-22                       | 479                        | -266                                     |
|       |        | 15.6       | 1.37E-19                   | 6.61E-22                       | 496                        | -225                                     |
|       |        | 18.7       | 5.04E-20                   | 4.66E-22                       | 483                        | -187                                     |
| 6     | 45     | 10.5       | 1.01E-19                   | 1.14E-21                       | 533                        | -128                                     |
|       |        | 12.4       | 5.01E-21                   | 3.93E-22                       | 572                        | -161                                     |
|       |        | 12.8       | 8.57E-20                   | 3.65E-22                       | 490                        | -202                                     |
|       |        | 15.6       | 2.38E-19                   | 8.24E-22                       | 481                        | -161                                     |
|       |        | 18.7       | 1.74E-19                   | 1.39E-21                       | 506                        | -141                                     |
| 7     | 214    | 10.5       | 5.42E-21                   | 3.25E-22                       | 589                        | -58                                      |
|       |        | 12.4       | 1.97E-21                   | 3.63E-22                       | 743                        | -111                                     |
|       |        | 12.8       | 5.43E-20                   | 3.26E-22                       | 481                        | -135                                     |
|       |        | 15.6       | 1.53E-20                   | 1.75E-22                       | 456                        | -97                                      |
|       |        | 18.7       | 5.18E-20                   | 3.16E-22                       | 519                        | -85                                      |
| 8     | 33     | 10.5       | 1.22E-20                   | 3.51E-22                       | 519                        | -93                                      |
|       |        | 12.4       | 1.27E-21                   | 2.16E-22                       | 513                        | -120                                     |
|       |        | 12.8       | 3.54E-20                   | 2.64E-22                       | 469                        | -192                                     |
|       |        | 15.6       | 3.30E-20                   | 1.37E-22                       | 458                        | -143                                     |
|       |        | 18.7       | 4.91E-20                   | 4.52E-22                       | 508                        | -135                                     |
| 9     | 42     | 10.5       | 5.73E-21                   | 4.82E-22                       | 590                        | -19                                      |
|       |        | 12.4       | 8.81E-22                   | 2.58E-22                       | 534                        | -133                                     |
|       |        | 12.8       | 2.63E-20                   | 2.56E-22                       | 501                        | -158                                     |
|       |        | 15.6       | 1.90E-20                   | 3.07E-22                       | 495                        | -89                                      |
|       |        | 18.7       | 2.56E-20                   | 2.93E-22                       | 532                        | -124                                     |

Table 2—Continued

| Order | Source | Line<br>μm | Flux<br>W cm <sup>-2</sup> | 1σ error<br>W cm <sup>-2</sup> | FWHM<br>km s <sup>-1</sup> | V <sub>helio</sub><br>km s <sup>-1</sup> |
|-------|--------|------------|----------------------------|--------------------------------|----------------------------|--|
| 10    | 32     | 10.5       | 2.38E-21                   | 2.40E-22                       | 592                        | 129                                      |
|       |        | 12.4       | 9.26E-22                   | 1.75E-22                       | 558                        | -100                                     |
|       |        | 12.8       | 2.27E-20                   | 2.19E-22                       | 531                        | -134                                     |
|       |        | 15.6       | 1.25E-20                   | 1.56E-22                       | 495                        | -108                                     |
|       |        | 18.7       | 1.48E-20                   | 4.15E-22                       | 651                        | -135                                     |
| 11    | 251    | 10.5       | 1.57E-20                   | 4.39E-22                       | 534                        | -12                                      |
|       |        | 12.4       | 1.41E-21                   | 1.97E-22                       | 439                        | -74                                      |
|       |        | 12.8       | 1.89E-20                   | 1.32E-22                       | 511                        | -86                                      |
|       |        | 15.6       | 3.99E-20                   | 3.12E-22                       | 480                        | -57                                      |
|       |        | 18.7       | 3.02E-20                   | 1.63E-21                       | 526                        | -43                                      |
| 12    | 62     | 10.5       | 2.97E-21                   | 3.21E-22                       | 565                        | -123                                     |
|       |        | 12.4       | 1.71E-21 <sup>a</sup>      | 6.12E-22                       | 848                        | -479                                     |
|       |        | 12.8       | 4.00E-20                   | 2.48E-22                       | 488                        | -237                                     |
|       |        | 15.6       | 1.05E-20                   | 1.29E-22                       | 473                        | -146                                     |
|       |        | 18.7       | 3.31E-20                   | 2.20E-22                       | 510                        | -173                                     |
| 13    | 27     | 10.5       | 8.79E-22                   | 1.87E-22                       | 644                        | 37                                       |
|       |        | 12.4       |                            |                                |                            |  |
|       |        | 12.8       | 8.47E-21                   | 8.19E-23                       | 524                        | -154                                     |
|       |        | 15.6       | 3.75E-21                   | 1.81E-22                       | 499                        | -106                                     |
|       |        | 18.7       | 8.07E-21                   | 2.23E-22                       | 514                        | -90                                      |
| 14    | 301    | 10.5       | 4.75E-21                   | 4.39E-22                       | 639                        | -132                                     |
|       |        | 12.4       | 1.29E-21                   | 1.78E-22                       | 471                        | -210                                     |
|       |        | 12.8       | 5.04E-20                   | 5.64E-22                       | 476                        | -226                                     |
|       |        | 15.6       | 1.46E-20                   | 2.55E-22                       | 480                        | -167                                     |
|       |        | 18.7       | 4.69E-20                   | 5.63E-22                       | 493                        | -172                                     |
| 15    | 4      | 10.5       | 1.46E-20                   | 4.34E-22                       | 524                        | -159                                     |
|       |        | 12.4       | 2.52E-21                   | 2.84E-22                       | 778                        | -258                                     |
|       |        | 12.8       | 6.00E-20                   | 2.32E-22                       | 466                        | -240                                     |
|       |        | 15.6       | 4.35E-20                   | 2.15E-21                       | 463                        | -200                                     |
|       |        | 18.7       | 7.80E-20                   | 5.68E-22                       | 507                        | -190                                     |
| 16    | 79     | 10.5       | 7.70E-20                   | 1.26E-21                       | 568                        | -226                                     |
|       |        | 12.4       | 4.23E-21                   | 7.16E-22                       | 427                        | -283                                     |
|       |        | 12.8       | 1.58E-19                   | 1.24E-21                       | 449                        | -331                                     |
|       |        | 15.6       | 1.99E-19                   | 6.83E-22                       | 489                        | -221                                     |
|       |        | 18.7       | 2.31E-19                   | 1.40E-21                       | 508                        | -236                                     |
| 17    | 87E    | 10.5       | 5.29E-21                   | 4.49E-22                       | 582                        | -166                                     |
|       |        | 12.4       | 1.31E-21                   | 3.21E-22                       | 638                        | -392                                     |
|       |        | 12.8       | 4.87E-20                   | 2.81E-22                       | 449                        | -148                                     |
|       |        | 15.6       | 1.82E-20                   | 2.51E-22                       | 463                        | -193                                     |
|       |        | 18.7       | 4.91E-20                   | 4.06E-22                       | 507                        | -184                                     |
| 18    | 302    | 10.5       | 7.26E-21                   | 1.76E-22                       | 410                        | -227                                     |
|       |        | 12.4       | 1.36E-21                   | 2.47E-22                       | 565                        | -326                                     |
|       |        | 12.8       | 4.21E-20                   | 1.93E-22                       | 438                        | -299                                     |
|       |        | 15.6       | 1.80E-20                   | 1.29E-22                       | 464                        | -232                                     |
|       |        | 18.7       | 3.98E-20                   | 1.92E-22                       | 496                        | -246                                     |

Table 2—Continued

| Order | Source | Line<br>μm | Flux<br>W cm <sup>-2</sup> | 1σ error<br>W cm <sup>-2</sup> | FWHM<br>km s <sup>-1</sup> | V <sub>helio</sub><br>km s <sup>-1</sup> |
|-------|--------|------------|----------------------------|--------------------------------|----------------------------|--|
| 19    | 702    | 10.5       | 8.60E-22                   | 2.62E-22                       | 533                        | 374                                      |
|       |        | 12.4       |                            |                                |                            |  |
|       |        | 12.8       | 4.67E-21                   | 1.62E-22                       | 576                        | -104                                     |
|       |        | 15.6       | 8.13E-22                   | 2.00E-22                       | 903                        | -69                                      |
|       |        | 18.7       | 3.03E-21                   | 1.86E-22                       | 574                        | -95                                      |
| 20    | 95     | 10.5       | 6.95E-21                   | 3.86E-22                       | 595                        | -118                                     |
|       |        | 12.4       | 8.60E-22                   | 1.82E-22                       | 462                        | -236                                     |
|       |        | 12.8       | 3.23E-20                   | 2.35E-22                       | 473                        | -215                                     |
|       |        | 15.6       | 2.13E-20                   | 2.56E-22                       | 471                        | -163                                     |
|       |        | 18.7       | 3.68E-20                   | 3.98E-22                       | 532                        | -161                                     |
| 21    | 710    | 10.5       | 6.59E-21                   | 5.02E-22                       | 647                        | -66                                      |
|       |        | 12.4       | 2.13E-21                   | 3.88E-22                       | 893                        | -84                                      |
|       |        | 12.8       | 3.48E-20                   | 4.07E-22                       | 515                        | -155                                     |
|       |        | 15.6       | 1.72E-20                   | 2.00E-22                       | 522                        | -108                                     |
|       |        | 18.7       | 4.05E-20                   | 4.90E-22                       | 554                        | -119                                     |
| 22    | 88W    | 10.5       | 1.55E-20                   | 3.34E-22                       | 548                        | -143                                     |
|       |        | 12.4       |                            |                                |                            |  |
|       |        | 12.8       | 2.29E-20                   | 1.26E-22                       | 444                        | -196                                     |
|       |        | 15.6       | 4.01E-20                   | 2.46E-22                       | 470                        | -163                                     |
|       |        | 18.7       | 4.06E-20                   | 4.21E-22                       | 521                        | -159                                     |
| 23    | 691    | 10.5       | 4.43E-20                   | 5.36E-22                       | 509                        | -238                                     |
|       |        | 12.4       | 1.67E-21                   | 3.42E-22                       | 655                        | -406                                     |
|       |        | 12.8       | 3.35E-20                   | 2.99E-22                       | 489                        | -286                                     |
|       |        | 15.6       | 9.60E-20                   | 4.39E-22                       | 488                        | -242                                     |
|       |        | 18.7       | 6.43E-20                   | 5.49E-22                       | 504                        | -226                                     |
| 24    | 651    | 10.5       | 5.67E-21                   | 2.63E-22                       | 541                        | -195                                     |
|       |        | 12.4       |                            |                                |                            |  |
|       |        | 12.8       | 5.93E-21                   | 1.67E-22                       | 575                        | -276                                     |
|       |        | 15.6       | 1.43E-20                   | 1.20E-22                       | 509                        | -199                                     |
|       |        | 18.7       | 7.97E-21                   | 1.63E-22                       | 544                        | -258                                     |
| 25    | 740W   | 10.5       | 2.29E-21                   | 1.90E-22                       | 375                        | -146                                     |
|       |        | 12.4       |                            |                                |                            |  |
|       |        | 12.8       | 1.77E-20                   | 2.60E-22                       | 482                        | -224                                     |
|       |        | 15.6       | 1.09E-20                   | 1.58E-22                       | 468                        | -179                                     |
|       |        | 18.7       | 2.02E-20                   | 2.99E-22                       | 504                        | -164                                     |

<sup>a</sup> Flux less than 3σ, not used in the analysis

Table 3. Derived Parameters for the H II Regions in M33

| Source | $R_G$<br>kpc | $\frac{Ne^+}{H^+}$<br>$(\times 10^{-6})$ | $\frac{Ne^{++}}{H^+}$<br>$(\times 10^{-6})$ | $\frac{S^{++}}{H^+}$<br>$(\times 10^{-6})$ | $\frac{S^{3+}}{H^+}$<br>$(\times 10^{-8})$ | $\frac{Ne^+}{S^{++}}$ | $\frac{Ne^{++}}{S^{++}}$ | $\frac{Ne^{++}}{Ne^+}$ | $\frac{S^{3+}}{S^{++}}$ | $\frac{Ne}{S}$ | $\frac{<S^{++}>}{<Ne^+>}$ | $\frac{<Ne^{++}>}{<S^{++}>}$ | $\frac{<Ne^{++}>}{<S^{3+}>}$ |           |
|--------|--------------|--|---|--|--|-----------------------|--------------------------|------------------------|-------------------------|----------------|---------------------------|------------------------------|------------------------------|-----------|
| 1      | 280          | 5.76                                     |   |  |  | 3.97±0.06             | 12.6±0.1                 | 3.17±0.04              | 0.245±0.004             | 13.3±0.1       | 3.60±0.06                 | 0.881±0.010                  | 3.60±0.05                    |           |
| 2      | 230          | 4.11                                     |   |  |  | 31.0±2.1              | 1.79±0.54                | 0.0575±0.0170          |                         | 32.8±2.3       | 0.460±0.031               | 0.125±0.038                  |                              |           |
| 3      | 277          | 3.37                                     |   |  |  | 7.40±0.20             | 6.90±0.15                | 0.932±0.017            | 0.104±0.007             | 12.9±0.3       | 1.93±0.05                 | 0.483±0.010                  | 4.63±0.27                    |           |
| 4      | 638          | 6.73                                     | 8.35±1.40                                   | 31.3±5.2                                   | 2.13±0.35                                  | 72.1±12.0             | 3.93±0.08                | 14.7±0.2               | 3.74±0.07               | 0.339±0.006    | 13.9±0.1                  | 3.64±0.08                    | 1.03±0.01                    | 3.04±0.04 |
| 5      | 623          | 5.70                                     | 14.7±1.7                                    | 28.4±3.3                                   | 1.59±0.18                                  | 49.9±5.8              | 9.27±0.21                | 17.9±0.2               | 1.93±0.04               | 0.314±0.005    | 20.7±0.2                  | 1.54±0.04                    | 1.25±0.01                    | 3.99±0.05 |
| 6      | 45           | 2.04                                     | 34.1±4.0                                    | 41.3±4.8                                   | 4.61±0.54                                  | 56.5±6.6              | 7.39±0.07                | 8.96±0.08              | 1.21±0.01               | 0.123±0.002    | 14.6±0.1                  | 1.93±0.02                    | 0.627±0.005                  | 5.12±0.06 |
| 7      | 214          | 2.25                                     | 55.0±11.2                                   | 6.75±1.37                                  | 3.49±0.71                                  | 7.75±1.64             | 15.8±0.1                 | 1.93±0.02              | 0.123±0.002             | 0.0222±0.0013  | 17.3±0.1                  | 0.906±0.008                  | 0.135±0.002                  | 6.09±0.37 |
| 8      | 33           | 1.32                                     | 55.5±10.6                                   | 22.6±4.3                                   | 5.12±0.98                                  | 27.0±5.2              | 10.8±0.1                 | 4.41±0.04              | 0.407±0.003             | 0.0527±0.0016  | 14.5±0.1                  | 1.32±0.02                    | 0.309±0.003                  | 5.86±0.17 |
| 9      | 42           | 1.36                                     | 59.5±18.2                                   | 18.8±5.7                                   | 3.86±1.18                                  | 18.3±5.8              | 15.4±0.2                 | 4.87±0.10              | 0.315±0.006             | 0.0475±0.0040  | 19.4±0.3                  | 0.925±0.014                  | 0.341±0.007                  | 7.18±0.62 |
| 10     | 32           | 1.28                                     | 48.9±10.3                                   | 11.8±2.5                                   | 2.12±0.45                                  | 7.25±1.68             | 23.1±0.7                 | 5.56±0.17              | 0.241±0.004             | 0.0342±0.0036  | 27.7±0.8                  | 0.619±0.018                  | 0.390±0.012                  | 11.4±1.2  |
| 11     | 251          | 5.10                                     | 26.7±4.4                                    | 24.6±4.0                                   | 2.84±0.49                                  | 31.4±5.2              | 9.40±0.50                | 8.67±0.46              | 0.922±0.010             | 0.111±0.007    | 16.3±0.8                  | 1.52±0.08                    | 0.607±0.032                  | 5.49±0.16 |
| 12     | 62           | 1.72                                     |   |  |  | 18.1±0.2              | 2.08±0.03                | 0.115±0.002            | 0.0191±0.0021           | 19.8±0.2       | 0.787±0.007               | 0.146±0.002                  | 7.68±0.83                    |           |
| 13     | 27           | 0.712                                    |   |  |  | 15.8±0.4              | 3.05±0.17                | 0.193±0.010            | 0.0231±0.0050           | 18.4±0.5       | 0.905±0.026               | 0.214±0.012                  | 9.23±2.01                    |           |
| 14     | 301          | 1.53                                     | 78.0±12.7                                   | 9.89±1.61                                  | 4.83±0.79                                  | 10.4±1.9              | 16.2±0.3                 | 2.05±0.04              | 0.127±0.003             | 0.0215±0.0020  | 17.8±0.3                  | 0.884±0.014                  | 0.143±0.003                  | 6.66±0.63 |
| 15     | 4            | 1.53                                     | 47.4±6.7                                    | 15.0±2.2                                   | 4.10±0.58                                  | 16.4±2.4              | 11.6±0.1                 | 3.66±0.18              | 0.317±0.016             | 0.0399±0.0012  | 14.6±0.2                  | 1.23±0.01                    | 0.257±0.013                  | 6.43±0.37 |
| 16     | 79           | 0.747                                    | 74.4±14.1                                   | 41.1±7.8                                   | 7.25±1.38                                  | 51.3±9.8              | 10.3±0.1                 | 5.67±0.04              | 0.553±0.005             | 0.0708±0.0012  | 14.9±0.1                  | 1.39±0.01                    | 0.397±0.003                  | 5.61±0.09 |
| 17     | 87E          | 1.12                                     | 74.2±19.3                                   | 12.1±3.2                                   | 4.98±1.30                                  | 11.4±3.1              | 14.9±0.1                 | 2.43±0.04              | 0.163±0.002             | 0.0229±0.0019  | 16.9±0.2                  | 0.959±0.009                  | 0.170±0.003                  | 7.44±0.64 |
| 18     | 302          | 2.09                                     | 61.7±12.4                                   | 11.6±2.3                                   | 3.89±0.78                                  | 15.1±3.1              | 15.9±0.1                 | 2.97±0.03              | 0.187±0.002             | 0.0387±0.0010  | 18.1±0.1                  | 0.900±0.006                  | 0.208±0.002                  | 5.37±0.14 |
| 19     | 702          | 3.27                                     |   |  |  | 23.2±1.6              | 1.76±0.45                | 0.0761±0.0189          | 0.0604±0.0188           | 23.5±1.6       | 0.616±0.042               | 0.123±0.031                  | 2.04±0.80                    |           |
| 20     | 95           | 2.34                                     | 74.8±17.1                                   | 21.6±5.0                                   | 5.68±1.30                                  | 22.8±5.4              | 13.2±0.2                 | 3.80±0.06              | 0.289±0.004             | 0.0401±0.0023  | 16.3±0.2                  | 1.08±0.01                    | 0.266±0.004                  | 6.65±0.38 |
| 21     | 710          | 3.10                                     | 32.6±6.6                                    | 7.04±1.42                                  | 2.53±0.51                                  | 8.73±1.88             | 12.9±0.2                 | 2.78±0.05              | 0.216±0.004             | 0.0345±0.0027  | 15.2±0.2                  | 1.11±0.02                    | 0.195±0.003                  | 5.65±0.44 |
| 22     | 88W          | 2.52                                     |   |  |  | 8.48±0.10             | 6.48±0.08                | 0.765±0.006            | 0.0811±0.0019           | 13.8±0.1       | 1.68±0.02                 | 0.454±0.005                  | 5.60±0.13                    |           |
| 23     | 651          | 4.77                                     |   |  |  | 11.2±0.4              | 11.8±0.3                 | 1.05±0.03              | 0.151±0.008             | 19.9±0.5       | 1.28±0.04                 | 0.823±0.018                  | 5.45±0.26                    |           |
| 24     | 691          | 3.29                                     | 39.9±8.8                                    | 49.9±11.1                                  | 5.10±1.13                                  | 74.5±16.5             | 7.83±0.10                | 9.79±0.09              | 1.25±0.01               | 0.146±0.002    | 15.4±0.1                  | 1.82±0.02                    | 0.686±0.006                  | 4.69±0.06 |
| 25     | 740W         | 4.12                                     |   |  |  | 13.2±0.3              | 3.53±0.07                | 0.268±0.006            | 0.0241±0.0020           | 16.3±0.3       | 1.08±0.02                 | 0.247±0.005                  | 10.3±0.9                     |           |

Table 4. Models Varying the Nebular Parameters

| Model | Symbol   | $T_{\text{eff}}$<br>(K) | DENS<br>(cm $^{-3}$ ) | $R_{\text{init}}$<br>(pc) | $N_{\text{Lyc}}$<br>(s $^{-1}$ ) | Abundances  |
|-------|----------|-------------------------|-----------------------|---------------------------|----------------------------------|-------------|
| 1     | asterisk | 35000                   | 1000                  | 0.5                       | $10^{49}$                        | reference   |
| 2     | triangle | 35000                   | 100                   | 0.0                       | $10^{49}$                        | reference   |
| 3     | X        | 35000                   | 100                   | 0.0                       | $10^{50}$                        | reference   |
| 4     | square   | 35000                   | 1000                  | 0.0                       | $10^{49}$                        | reference/3 |
| 5     | asterisk | 40000                   | 1000                  | 0.5                       | $10^{49}$                        | reference   |
| 6     | triangle | 40000                   | 100                   | 0.0                       | $10^{49}$                        | reference   |
| 7     | X        | 40000                   | 100                   | 0.0                       | $10^{50}$                        | reference   |
| 8     | square   | 40000                   | 1000                  | 0.0                       | $10^{49}$                        | reference/3 |
| 9     | asterisk | 45000                   | 1000                  | 0.5                       | $10^{49}$                        | reference   |
| 10    | triangle | 45000                   | 100                   | 0.0                       | $10^{49}$                        | reference   |
| 11    | X        | 45000                   | 100                   | 0.0                       | $10^{50}$                        | reference   |
| 12    | square   | 45000                   | 1000                  | 0.0                       | $10^{49}$                        | reference/3 |

Table 5. Blue Compact Dwarf Galaxy Results

| Object  | $T_e$ & $N_e$ from Wu et al. (2008) Table 2 |                      |          | $T_e = 10000$ K & $N_e = 100$ cm $^{-3}$ |                      |           |
|---------|---|----------------------|----------|--|----------------------|-----------|
|         | Ne $^{++}$ /Ne $^{+}$                       | S $^{3+}$ /S $^{++}$ | Ne/S     | Ne $^{++}$ /Ne $^{+}$                    | S $^{3+}$ /S $^{++}$ | Ne/S      |
| Haro11  | 1.41±0.01                                   | 0.194±0.001          | 19.6±0.1 | 1.38±0.01                                | 0.200±0.001          | 20.1±0.1  |
| NGC1140 | 1.45±0.03                                   | 0.125±0.001          | 18.3±0.2 | 1.45±0.03                                | 0.125±0.001          | 18.3±0.2  |
| NGC1569 | 4.97±0.06                                   | 0.421±0.002          | 13.4±0.1 | 4.91±0.06                                | 0.418±0.002          | 13.3±0.1  |
| IZW40   | 8.07±0.15                                   | 0.881±0.009          | 10.0±0.1 | 7.91±0.15                                | 0.837±0.009          | 9.74±0.08 |
| UGC4274 | 0.634±0.010                                 | 0.0666±0.0020        | 15.5±0.2 | 0.634±0.010                              | 0.0683±0.0020        | 15.8±0.2  |
| IZW18   | 2.33±0.28                                   | 0.456±0.048          | 13.2±1.0 | 2.24±0.27                                | 0.431±0.045          | 13.1±1.0  |
| Mrk1450 | 3.19±0.07                                   | 0.350±0.003          | 14.0±0.1 | 3.14±0.07                                | 0.347±0.003          | 13.9±0.1  |
| UM461   | 7.99±1.00                                   | 1.25±0.05            | 12.0±0.3 | 7.75±0.97                                | 1.16±0.04            | 11.7±0.3  |
| Mrk1499 | 1.22±0.02                                   | 0.147±0.002          | 18.5±0.2 | 1.17±0.02                                | 0.123±0.002          | 18.4±0.2  |

Table 6. NGC 3603, 30 Doradus, N 66 Results

| Object     | $\text{Ne}^{++}/\text{Ne}^+$ | $\text{S}^{3+}/\text{S}^{++}$ | $\text{Ne}/\text{S}$ |
|------------|------------------------------|-------------------------------|----------------------|
| NGC 3603#3 | 0.596                        | 0.0953                        | 23.4                 |
| NGC 3603#4 | 0.257                        | 0.0312                        | 14.6                 |
| NGC 3603#5 | 0.953                        | 0.101                         | 13.0                 |
| 30 Dor#2   | 1.72                         | 0.0913                        | 11.9                 |
| 30 Dor#3   | 3.30                         | 0.197                         | 11.2                 |
| 30 Dor#4   | 5.98                         | 0.398                         | 10.8                 |
| 30 Dor#5   | 1.55                         | 0.103                         | 11.7                 |
| 30 Dor#6   | 2.06                         | 0.129                         | 11.3                 |
| 30 Dor#7   | 4.19                         | 0.274                         | 11.3                 |
| 30 Dor#8   | 0.791                        | 0.0590                        | 13.4                 |
| 30 Dor#10  | 0.351                        | 0.0517                        | 13.8                 |
| 30 Dor#11  | 2.29                         | 0.122                         | 11.3                 |
| 30 Dor#12  | 3.27                         | 0.234                         | 11.4                 |
| 30 Dor#13  | 2.50                         | 0.147                         | 10.9                 |
| 30 Dor#14  | 3.28                         | 0.230                         | 12.1                 |
| 30 Dor#15  | 3.80                         | 0.219                         | 11.5                 |
| 30 Dor#16  | 5.64                         | 0.318                         | 10.8                 |
| 30 Dor#17  | 0.400                        | 0.0353                        | 15.2                 |
| N 66#1     | 4.65                         | 0.285                         | 8.97                 |
| N 66#2     | 3.83                         | 0.294                         | 9.40                 |
| N 66#5     | 3.81                         | 0.240                         | 9.95                 |
| N 66#6     | 1.71                         | 0.250                         | 10.4                 |
| N 66#7     | 5.24                         | 0.252                         | 9.25                 |
| N 66#8     | 2.27                         | 0.194                         | 10.7                 |
| N 66#9     | 2.05                         | 0.164                         | 11.2                 |
| N 66#10    | 2.04                         | 0.167                         | 11.3                 |
| N 66#11    | 2.03                         | 0.160                         | 10.9                 |
| N 66#12    | 5.33                         | 0.447                         | 10.1                 |
| N 66#13    | 3.37                         | 0.225                         | 9.80                 |